Czech Technical University in Prague
Faculty of Nuclear Sciences and Physical Engineering
Department of Physics

Programme: Mathematical Engineering
Branch of Study: Mathematical Physics

High pT jets in RunII of the ATLAS Experiment

MASTER'S DEGREE PROJECT

Author: Jan Lochman
Supervisor: Ing. Zdeněk Hubáček, Ph.D.
Submitted in: May 2015

Zadani prace

Statement

Prohlasuji…

V Praze dne ....

Jan Lochman

Acknowledgment

Dekuji. . .

Jan Lochman

Název práce:
Jety s vysokou příčnou hybností v RunII experimentu ATLAS

Autor: Jan Lochman

Obor: Matematické Inženýrství

Druh práce: Diplomová práce

Vedoucí práce: Ing. Zdeněk Hubáček, Ph.D.
CERN

Abstrakt: Abstrakt CZ

Klíčová slova: Klicova slova

Title:
High pT jets in RunII of the ATLAS Experiment

Author: Jan Lochman

Abstract: Abstrakt EN

Key words: Key words

Contents

Introduction

Chapter 1

QCD

Is the purpose of theoretical physics to be no more than a cataloging of all the things that can happen when particles interact with each other and separate? Or is it to be an understanding at a deeper level in which there are things that are not directly observable (as the underlying quantized fields are) but in terms of which we shall have a more fundamental understanding?

Julian Schwinger

The theoretical framework of particle physics is called the Standard Model (SM). The SM describes the way how the fundamental components of matter interact with each other through strong, weak and electromagnetic interactions. Mathematically the SM is gauge quantum field theory with local internal symmetries of the direct product group $SU(3) \times SU(2) \times U(1)$. Gauge bosons are assigned to generators of this symmetry - there are 8 massless gluons from $SU(3)$ and 3 massive $W^{\pm}, Z$ bosons with 1 massless boson γ from electroweak $SU(2) \times U(1)$ sector. Higgs mechanism has to be introduced in the electroweak sector to assign $W^{\pm}, Z$ bosons mass and as consequence the new particle - Higgs boson - emerges in the SM theory. All bosons have integer spin.

In addition to the bosons the SM introduces spin1/2 fermions which are divided into three quark and three lepton families. Fermions are assumed to be point-like because there is no evidence for their internal structure to date. All fermions interact weakly, if they have electrical charge, they interact electromagnetically as well. Quarks are the only fundamental fermions which do interact strongly. System of fundamental particles of the SM is shown in Figure 1.1.

Quarks bind together to form hadrons and there are hundreds (?source?) of known hadrons up to date. Hadrons are divided into baryons (3 quarks) and mesons (quark and anti-quark pairs). Theory describing the interaction between quarks is called Quantum Chromodynamics (QCD) which key features will be discussed in this chapter. The reasoning for quark existence and for the description their strong interaction as $SU(3)$

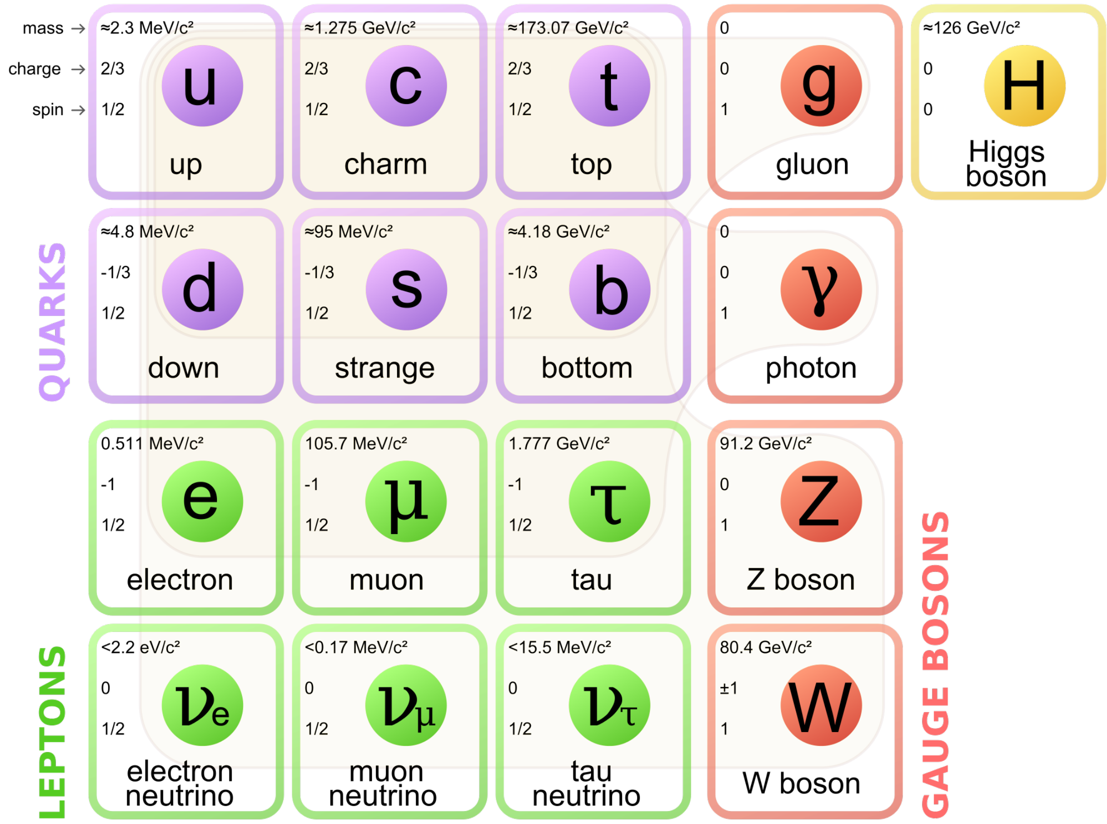

Figure 1.1: The system of fundamental particles of the SM. Figure from [1]

gauge theory will be presented. Running coupling constant will be discussed to split QCD into perturbative and non-perturbative regions - two regions, where QCD has to use different mathematical approach for the description of strong interaction. Most of ideas presented here is overtaken from the following textbook [2]. Electroweak sector of the SM is described in [3]. For more concise information about the SM the following textbooks can serve [4, 5].

1.1 Theoretical Ansatz

In 1950s, there have already been discovered tens of new hadrons thanks to new particle accelerators and a lot of effort was exerted to categorize them. To each particle there was assigned a series of quantum numbers including isospin T with its third component T_3, hypercharge Y, electrical charge Q, strangeness S, baryon number B and others. Soon it was recognized, that there are some symmetries between these quantum numbers, like famous Gell-Mann–Nishijima relation [6, 7]

$$Q = T_3 + 1/2Y \quad , \quad Y = B + S + \dots , \tag{1.1}$$

	S	Y	T	T_3	Q
p	0	1	1/2	1/2	1
n				-1/2	0
Σ^+	-1	0	1	1	1
Σ^0				0	0
Σ^-				-1	-1
Λ			0	0	0
Ξ^0	-2	-1	1/2	1/2	0
Ξ^-				-1/2	-1

Table 1.1: Quantum numbers of selected baryons known in 1950s. S strangeness, Y hypercharge, T isospin, T_3 third component of isospin, Q electrical charge.

where dots denote charm, bottomness and topness and were introduced after work of Gell-Mann and Nishijima. Some of the baryons known by then are shown in table 1.1. In 1960s, the known hadrons were successfully categorized with the so called Eightfold Way, which was published independently by Murray Gell-Mann [8] and George Zweig [9] in 1964. The Eightfold Way successfully predicted the existence of new particle Ω^- including its mass. Basic ideas of Eightfold way will be discussed in this section.

The key feature of Eightfold Way is to understand hadrons as the part of different representations of infinitesimal generators of $SU(3)$ flavor symmetry group. These infinitesimal generators of $SU(3)$ form the real eight-dimensional Lie algebra $\mathfrak{su}(3)$ which fundamental representation is usually derived from Gell-Mann matrices

$$\begin{aligned}
&\lambda_1 = \begin{pmatrix} 0 & 1 & 0 \\ 1 & 0 & 0 \\ 0 & 0 & 0 \end{pmatrix} \quad \lambda_2 = \begin{pmatrix} 0 & -i & 0 \\ i & 0 & 0 \\ 0 & 0 & 0 \end{pmatrix} \quad \lambda_3 = \begin{pmatrix} 1 & 0 & 0 \\ 0 & -1 & 0 \\ 0 & 0 & 0 \end{pmatrix} \\
&\lambda_4 = \begin{pmatrix} 0 & 0 & 1 \\ 0 & 0 & 0 \\ 1 & 0 & 0 \end{pmatrix} \quad \lambda_5 = \begin{pmatrix} 0 & 0 & -i \\ 0 & 0 & 0 \\ i & 0 & 0 \end{pmatrix} \\
&\lambda_6 = \begin{pmatrix} 0 & 0 & 0 \\ 0 & 0 & 1 \\ 0 & 1 & 0 \end{pmatrix} \quad \lambda_7 = \begin{pmatrix} 0 & 0 & 0 \\ 0 & 0 & -i \\ 0 & i & 0 \end{pmatrix} \quad \lambda_8 = \frac{1}{\sqrt{3}} \begin{pmatrix} 1 & 0 & 0 \\ 0 & 1 & 0 \\ 0 & 0 & -2 \end{pmatrix} .
\end{aligned} \tag{1.2}$$

The generators are usually chosen $g_a = \frac{1}{2}\lambda_a$ and obey the commutation relation $[g_a, g_b] = i f_{abc} g_c$ with f_{abc} being structure constants. Cartan subalgebra of fundamental representation of $\mathfrak{su}(3)$ is generated by $H_1 = g_3$ and $H_2 = g_8$. The eigenstates of three-dimensional representation of $\mathfrak{su}(3)$ can be chosen

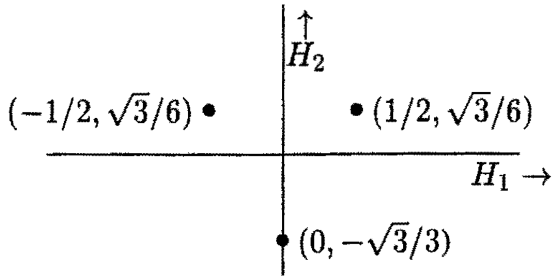

Figure 1.2: Eigenvalues of 3-dimensional representation of $\mathfrak{su}(3)$ Lie algebra. Figure from [10].

$$u = \begin{pmatrix} 1 \\ 0 \\ 0 \end{pmatrix} \leftrightarrow \left(\frac{1}{2}, \frac{\sqrt{3}}{6} \right), \quad d = \begin{pmatrix} 0 \\ 1 \\ 0 \end{pmatrix} \leftrightarrow \left(-\frac{1}{2}, \frac{\sqrt{3}}{6} \right), \quad s = \begin{pmatrix} 0 \\ 0 \\ 1 \end{pmatrix} \leftrightarrow \left(0, -\frac{\sqrt{3}}{3} \right), \tag{1.3}$$

where the eigenvalues to generators of the Cartan subalgebra was assigned $H_1 u = \frac{1}{2} u$, $H_2 u = \frac{\sqrt{3}}{6} u$ and similarly for d and s eigenstates. These eigenvalues are shown in Figure 1.2. Other important representation of $\mathfrak{su}(3)$ is eight-dimensional adjoint representation. This representation has the following eigenstates and corresponding eigenvalues

$$\begin{aligned} \frac{1}{\sqrt{2}} (g_1 \pm i g_2) &\leftrightarrow (\pm 1, 0), \\ \frac{1}{\sqrt{2}} (g_4 \pm i g_5) &\leftrightarrow \left(\pm \frac{1}{2}, \pm \frac{\sqrt{3}}{2} \right), \\ \frac{1}{\sqrt{2}} (g_6 \pm i g_7) &\leftrightarrow \left(\mp \frac{1}{2}, \pm \frac{\sqrt{3}}{2} \right), \end{aligned} \tag{1.4}$$

where again when denoting $A = \frac{1}{\sqrt{2}}(g_1 + i g_2)$ then the upper sign of the first expression reads $[H_1, A] = A$ and $[H_2, A] = 0$ and similarly for remaining 5 eigenstates. Defining

$$H_1 = T_3 \quad \text{and} \quad H_2 = \frac{\sqrt{3}}{2} Y \tag{1.5}$$

one can easily assign hadrons from table 1.1 to corresponding eigenvalues of adjoint representation in (1.4) according to its third component of isospin T_3 and its hypercharge Y. This is depicted in Figure 1.3.

When the same redefinition is done to the eigenstates of three-dimensional representation in (1.3), one can assign to eigenstates the hypercharge Y and strangeness S as well. The concrete values for states u, d, s are shown in table 1.2.

It is possible to find another representations of Lie algebra, to which the observed hadrons can be assigned. The simplest way seems to be through highest weight defining representation. From eigenvalues of adjoint representation (1.4) one can find simple roots $\alpha^1 = \left(\frac{1}{2}, \frac{\sqrt{3}}{2}\right)$, $\alpha^2 = \left(\frac{1}{2}, -\frac{\sqrt{3}}{2}\right)$, which are defining the highest weights $\mu^1 = \left(\frac{1}{2}, \frac{\sqrt{3}}{6}\right)$,

	S	Y	T	T_3	Q
u	0	1/3	1/2	1/2	2/3
d				-1/2	-1/3
s	-1	-2/3	0	0	

Table 1.2: Quantum numbers of three quarks which existence was predicted by Gell-Mann and Zweig in 1964.

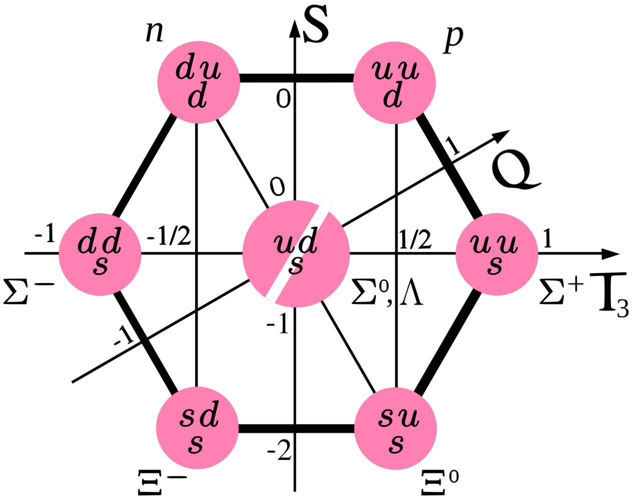

Figure 1.3: Baryonic octuplet encapsulating baryons from table 1.1. For baryons in this diagram, the relation $Y = S + 1$ holds. Figure from [11].

$\mu^2 = \left(\frac{1}{2}, -\frac{\sqrt{3}}{6}\right)$. New representation of Lie algebra can be constructed from highest weight. This procedure is described in [10] in detail.

Representations defined by highest weight μ^1 or μ^2 respectively are called fundamental. Fundamental representation defined by μ^1 is usually denoted $\mathbf{3}$ and was encountered already by expressions (1.3) with weight diagram at Figure 1.2, corresponding to three different quark states. The second fundamental representation corresponds to three anti-quark states and is usually denoted $\bar{\mathbf{3}}$. Representation depicted in Figure 1.3 is defined by the highest weight $\mu^1 + \mu^2$.

Special interest is in representations with dimensions 10 and 8. These are present in decompositions $\mathbf{3} \otimes \mathbf{3} \otimes \mathbf{3} = \mathbf{10} \oplus \mathbf{8} \oplus \mathbf{8} \oplus \mathbf{1}$, which correspond to the baryons composed of three quarks, and $\mathbf{3} \otimes \bar{\mathbf{3}} = \mathbf{8} \oplus \mathbf{1}$ corresponding to mesons from quark and anti-quark.

Important feature of quark model just presented is its capability to predict hadron masses. This is done using Gell-Mann–Okubo mass formula [12, 13]

$$M = a_0 + a_1 S + a_2 \left(T(T+1) - \frac{1}{4} S^2 \right), \tag{1.6}$$

where a_0, a_1 and a_2 are free parameters which are common for all hadrons in one multiplet.

In 1970 Sheldon Lee Glashow, John Iliopoulos and Luciano Maiani proposed [14] an extension which predicted existence of fourth flavor of quark - charm quark. In 1973 the Makoto Kobayashi and Toshihide Moskawa proposed [15] that the existence of 6 different quark flavors could explain the experimental observation of CP violation.

1.2 Experimental Ground

In the previous section it was shown the hadrons can be categorized using representations of $\mathfrak{su}(3)$ Lie algebra. This lead to the model, where baryons were composed of three quarks whereas the mesons of quark and anti-quark. In this section, some experimental evidences will be presented to support quark model. First the scattering reactions will be discussed. It will be shown, that the lepton scattering on nucleons can be explained by assumption, that nucleons are composed of point-like spin-1/2 particles. Next discussion will address the fact, that there are three color charges - this will encounter the question, why the group $SU(3)$ is connected to the theory of strong interaction.

1.2.1 Scattering Reactions

One of the possibilities, how to find out, if there is some inner structure in nucleon N, are the scattering reactions

$$e^- \,(E \gg 1\,\mathrm{GeV}) + N \to e^- + N, \tag{1.7}$$

$$\nu_e \,(E \gg 1\,\mathrm{GeV}) + N \to \nu_e + N, \tag{1.8}$$

where the condition $E \gg 1\,\mathrm{GeV}$ is explicitly written to ensure the wavelength of lepton being $< 0.2\,\mathrm{fm}$. By the first scattering reaction, the information about electric charge distribution in nucleon can be extracted, whereas the second scattering reaction informs us about weak charge distribution. Further only (1.7) will be discussed. Feynmann diagram of this process is depicted with kinematics variables and vertex algebraic structures in Figure 1.4.

Because of Lorentz-invariance of QED, the matrix element of the nucleon vertex $\bar{u}(P', S')\Gamma_\mu u(P, S)$ has to be a Lorentz-vector. This restricts the possible form of Γ_μ to the following algebraic structure

$$\Gamma_\mu = A\gamma_\mu + BP'_\mu + CP_\mu + iDP'^\nu\sigma_{\mu\nu} + iEP^\nu\sigma_{\mu\nu}, \tag{1.9}$$

where A,...,E depend only on Lorentz-invariant quantities. Next condition which has to be taken into account, is gauge invariance of matrix element, which can be written in the form

$$q^\mu \bar{u}(P', S')\Gamma_\mu u(P, S). \tag{1.10}$$

The further computation of cross section is straightforward and the result can be easily generalized to non-elastic scattering by which the nucleon in final state decays. The result is usually written using inelasticity parameter $y = \frac{E-E'}{E}$, $0 \le y \le 1$, $y = 0$

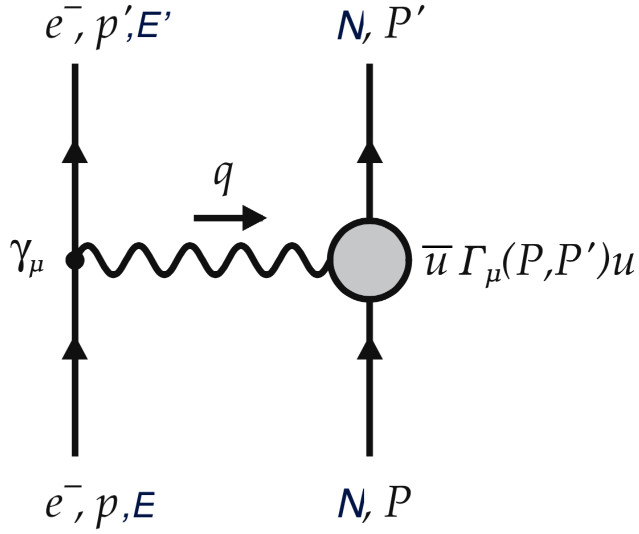

Figure 1.4: Scattering reaction $e^-N \to e^-N$ with kinematics variables and algebraic structures of vertices. Figure from [2].

corresponding to the elastic scattering, Bjorken variable $x = \frac{Q^2}{2P\cdot q}$, $0 < x \leq 1$, $x = 1$ denoting elastic scattering and finally instead of negative value q^2 the $Q^2 = -q^2$ is used. Final result can be than written in the form

$$\left.\frac{d^2\sigma}{dxdy}\right|_{eN} = \frac{8\pi M_N E\alpha^2}{Q^4}\left[xy^2F_1^{eN}(Q^2,x) + (1-y)F_2^{eN}(Q^2,x)\right]. \tag{1.11}$$

The eN sub(super)script stresses the fact, we are dealing with scattering (1.7). F_1^{eN} and F_2^{eN} are the so called structure functions, which are not determinable by the theory just presented - they have to be measured experimentally.

Structure constants were first measured by eP scattering at SLAC in 1968 [16] and shown the following results

1. for $Q^2 \geq 1\,\mathrm{GeV}$, there is no significant dependence of structure functions on Q^2 and
2. for $Q^2 \geq 1\,\mathrm{GeV}$, $F_2 \approx 2xF_1$.

These results can be explained by assumption nucleon being composed of point-like spin-1/2 constituents, for which R. P. Feynmann used term partons. In the following basic ideas of parton model will be presented. To ith parton, it is possible to assign momentum $P_{i,\xi}$

$$P_{i,\mu} = \xi_i P_\mu + \Delta P_{i,\mu} \quad , \quad \max_\mu(\Delta P_\mu) \ll \max_\mu P_\mu, \tag{1.12}$$

where $\xi_i \in \langle 0,1\rangle$ and $\Delta P_{i,\mu}$ comes from the interaction between partons and it is assumed, the momentum coming from this interaction is much smaller than the total nucleon momentum P_μ. In addition, probabilities $f_i(\xi_i)$ that ith parton will carry ξ_i fraction of total momentum fulfilling

$$\int d\xi_i f_i(\xi_i) = 1 \tag{1.13}$$

must be defined. Then for scattering reaction (1.7) the total cross section formula can be derived

$$\left.\frac{d^2\sigma}{dxdy}\right|_{eN} = \frac{4\pi M_N E\alpha^2}{Q^4}\left[y^2 + 2(1-y)\right]\sum_i f_i(x) q_i^2 x. \tag{1.14}$$

where for ith parton its electrical charge q_i was introduced. The last expression and (1.11) can be compared as polynomials in y resulting in

$$F_1^{eN}(x) = \frac{1}{2}\sum_i f_i(x) q_i^2 \quad , \quad F_2^{eN}(x) = \sum_i f_i(x) q_i^2 x. \tag{1.15}$$

It can be easily checked, that $F_2^{eN}(x) = 2xF_1^{eN}(x)$. Functions $f_i(x)$ just introduced are called Parton Distribution Functions (PDFs) and their important role in QCD will be discussed in (?somewhere?) in more details.

Important conclusion from analyzing of scattering reactions is, that the experimental results can be explained by assumption nucleons being composed of spin-1/2 point-like partons, now called quarks.

1.2.2 Number of Colors

Despite the strong confidence in the parton model, a theory which would describe the interaction between partons was still missing. There was no direct evidence on how the theory would look like at the beginning of 1970s. The theory of electroweak unification successfully suggested, that the gauge theories are the right theories for the description of our world at the subatomic level, but to construct gauge theory of strong interaction the number of colors first had to be known.

Number of colors N_C is the number of different kinds of quarks of the same flavor with respect to the new interaction. In this part, three arguments will be presented to demonstrate, that $N_C = 3$.

The first argument is the analysis of the electron-positron anihilation into the pair of fermion and anti-fermion

$$e^+e^- \to f\bar{f}. \tag{1.16}$$

Feynmann diagram of this reaction is shown in Figure 1.5a, where constants sitting in two vertices are empahised. α stands for fine structure constants and Q_f for charge of fermion f in units of positron charge. Total cross section has to be proportional to

$$\sigma(e^-e^+ \to f\bar{f}) \sim Q_f^2\alpha^2. \tag{1.17}$$

In the case fermion f being quark, there is new degeneracy in final state coming from different colors of quarks in final state - the total cross section has to be multiplied by factor N_C. Experimentally, the so called R-factor is measured

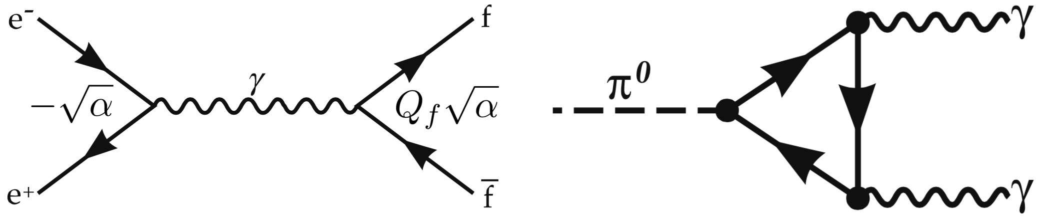

(a) $e^+e^- \to f\bar{f}$ (b) $\pi^0 \to 2\gamma$

Figure 1.5: (a) e^-e^+ annihilation itno the pair of fermion anti-fermion. Constants siting in both vertices are dented with α being the fine structure constant and Q_f the charge of fermion f in units of positron charge. (b) π^0 meson decay into pair of photons with closed fermion loop.

$$R = \frac{\sigma(e^+e^- \to \text{hadrons})}{\sigma(e^+e^- \to \mu^+\mu^-)} = \left(\sum_q Q_q^2\right) N_C, \tag{1.18}$$

where sum on the left hand side is over all possible quark states. When the quark model proposed by Gell-Mann a Zweig is used, then for the quark charges in table 1.2

$$R = \left[\left(\frac{2}{3}\right)^2 + \left(\frac{-1}{3}\right)^2 + \left(\frac{-1}{3}\right)^2\right] N_C = \frac{2}{3} N_C. \tag{1.19}$$

Experimental results for R-ratio have shown [17], that $N_C = 3$.

The second argument is the measurement of decay width of π_0 meson. Decay is depicted in Figure 1.5b. For decay width Γ it can be derived

$$\Gamma = 7.63 \left(\frac{N_C}{3}\right)^2 \text{ eV}, \tag{1.20}$$

which, compared to the experimental value $\Gamma = 7.57 \pm 0.32$ eV [17] leads again to $N_C = 3$.

The third argument is purely theoretical and states, that the SM is internally consistent only if there are three colors [2]. This indicates that there is some linking between electroweak and strong sector of SM and motivates the search for Grand Unified Theories.

1.3 QCD as a Gauge Theory

Putting arguments of previous section all together, there is strong experimental evidence, that nucleons consist of point-like spin-1/2 particles called quarks and that quarks bring into the theory new degeneracy factor $N_C = 3$, which can be understood as three different strong charges called colors.

Nowadays the quark-quark strong interaction is understood as an $SU(3)$ gauge theory in a degree of freedom called color. Gell-Mann matrices (1.2) can be chosen as generators of $SU(3)$. These matrices act on quark color triplets wave functions

$$\psi(x) = \begin{pmatrix} \psi_r(x) \\ \psi_g(x) \\ \psi_b(x) \end{pmatrix}. \tag{1.21}$$

Following the Yang-Mills theory [18], to each generator $\frac{\lambda^a}{2}$ gluon field $A^a_\mu(x)$ and gluon file strength tensor

$$F^a_{\mu\nu} = \left(\partial_\mu A^a_\nu - \partial_\nu A^a_\mu + g f^{abc} A^b_\mu A^c_\nu\right) \tag{1.22}$$

is assigned where g denotes the coupling constant of strong interaction and f^{abc} are structure constant defined in section 1.1. QCD Lagrangian

$$\mathscr{L}_{\text{QCD}} = \bar{\psi}\left(-i\partial_\mu + g\frac{\lambda}{2}A^a_\mu(x)\right)\gamma^\mu\psi - \frac{1}{4}F^a_{\mu\nu}F^{\mu\nu}_a \tag{1.23}$$

is invariant under local transformation

$$\begin{aligned} \psi(x) &\to \psi'(x) = \mathrm{e}^{ig\Theta(x)}\psi(x), \\ A_\mu(x) &\to \mathrm{e}^{ig\Theta(x)}\left(A_\mu(x) + \frac{i}{g}\partial_\mu\right)\mathrm{e}^{-ig\Theta(x)}, \end{aligned} \tag{1.24}$$

where

$$\Theta(x) = \frac{1}{2}\lambda^a\Theta^a(x) \quad , \quad A_\mu(x) = \frac{1}{2}\lambda^a A^a_\mu(x). \tag{1.25}$$

There is no mass term in Lagrangian (1.23) because mass term $m\bar{\psi}\psi$ vary under gauge transformation (1.24). Origin of mass term lies in Higgs mechanism [19] which is explained in [3] in details.

QCD Lagrangian (1.23) together with gauge transformations (1.24) are sufficient for determination of Feynman rules - key ingredient in perturbative QCD which will be discussed in next section.

By derivation of gluon propagator, one has to add to the QCD Lagrangain the so called gauge-fixing term

$$\mathscr{L}^{\text{gauge-fixing}}_{\text{QCD}} = -\frac{1}{2\xi}\left(\partial_\mu A^\mu_a\right)^2, \tag{1.26}$$

which confines the possible gauges to one class parametrized by real parameter ξ. In non-Abelian gauge theories this term must be supplemented by the so called ghost term which brings into the theory new unphysical scalar particle obeying fermionic statistics. More details on so called Faddev-Popov ghost filed can be found in [20].

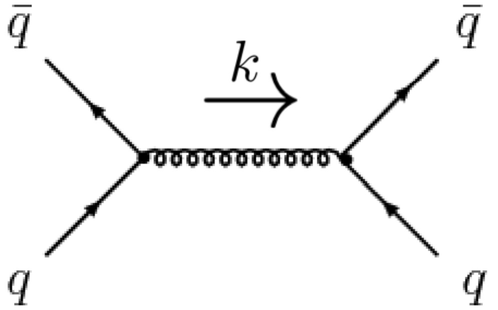

Figure 1.6: Leading order Feynmann diagrams in scattering reaction $q\bar{q} \to q\bar{q}$ with denoted transfered momentum k.

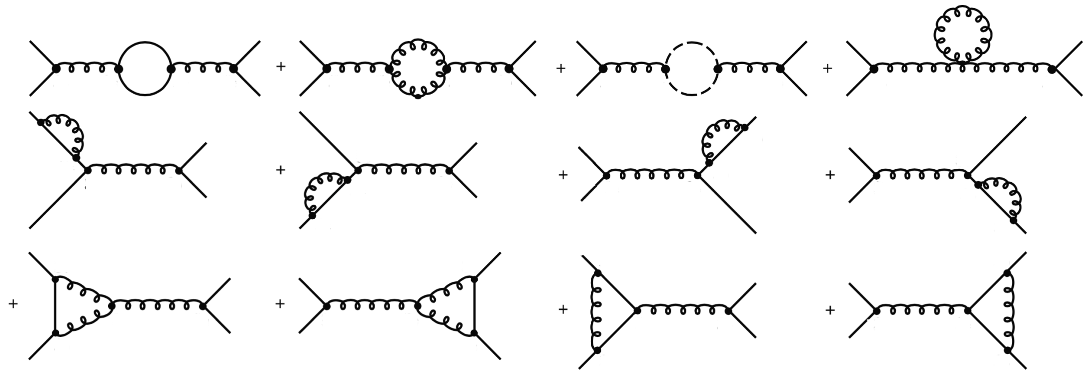

Figure 1.7: Next to the leading order Feynmann diagrams in scattering reactions $q\bar{q} \to q\bar{q}$. Dashed line represents scalar ghost particle.

1.4 Perturbative QCD

Quantum Electrodynamics (QED) and QCD are both quantum filed gauge theories, but they differ in one killing feature - the former is Abelian whereas the latter is not. The non-Abelian character of QCD leads to new phenomenons which have the origin in QCD Lagrangian (1.23) directly leading to triple and quartic gluonic interactions. In this section one remarkable consequence will be discussed - the running coupling constant.

Assume scattering process

$$q\bar{q} \to q\bar{q}, \tag{1.27}$$

which is depicted in the lowest order of perturbation theory by the Feynman graph in Figure 1.6. Except contribution of this graph to the scattering amplitude (which is the only contribution $\sim g^2$) there are 12 other Feynman diagrams with contributions $\sim g^4$. These are depicted in Figure 1.7.

The contributions from new Feynman diagrams are calculated in [2] in detail. There is shown, that all this contributions together are logarithmically divergent. This divergence can be removed, when from the scattering amplitude for arbitrary momentum transfer k^2 scattering amplitude for fixed momentum transfer $k^2 = -M^2$ is subtracted. This is how the renormalized coupling constant g_R is obtained and here is its final expression

$$g_R = g_0 - \frac{g_0^3}{16\pi^2}\left(\frac{11}{2} - \frac{1}{3}N_F\right)\ln\left(\frac{-k^2}{M^2}\right) + \mathscr{O}(g_0^5). \tag{1.28}$$

g_0 stands for the coupling constant measured at the renormalization scale $k^2 = -M^2$ and N_F is the number of different quark flavors with mass $m^2 \ll |k^2|$. Dependence of g_R on transfered momentum k^2 is evident, but there are another two intertwined dependences - on normalization scale M and on coupling constant at renormalization scale $g_0 = g_R|_{k^2=-M^2}$. For next purpose, it is convenient to use the dependence schema

$$g_R = g_R(-k^2, g_0(M)) \tag{1.29}$$

which allows the use of advantages of β-function and when the equation (1.28) is used, then the differential equation for $g_0(M)$ can be obtained

$$\beta(g_0) \equiv M\left(\frac{\partial g_R}{\partial M}\right)_{-k^2=M^2} = M\left(\frac{dg_0}{dM}\right)_{-k^2=M^2} \tag{1.30}$$

$$= -b_0 g_0^3 + \mathscr{O}(g_0^5), \quad b_0 = \frac{1}{16\pi^2}\left(11 - \frac{2N_F}{3}\right), \tag{1.31}$$

which can be solved directly to obtain coupling constant g_0 for arbitrary scale $-k^2$

$$\int_{g_0(M^2)}^{g_0(-k^2)} \frac{dg_0}{g_0^3} = -b_0 \int_{M^2}^{-k^2} \frac{dM}{M} \tag{1.32}$$

with solution

$$\alpha_S(-k^2) = \frac{\alpha_S(M^2)}{1 + \frac{\alpha_S(M^2)}{4\pi}\left(11 - \frac{2N_F}{3}\right)\ln\left(\frac{-k^2}{M^2}\right)}, \quad g_0^2(-k^2) = 4\pi\alpha_S(-k^2), \tag{1.33}$$

which is the final expression for running coupling constant up to one-loop order. This dependence corresponds to experimental data which are depicted in Figure 1.8. Coupling constant decreases with increasing momentum transfer allowing the use of the perturbation theory. This is known as Asymptotic Freedom [21].

On the other hand, when the momentum transfer decreases, there is special value $-k^2 = \Lambda^2$ for which the last expression diverges

$$-1 = \frac{\alpha_S(M^2)}{4\pi}\left(11 - \frac{2N_F}{3}\right)\ln\left(\frac{\Lambda^2}{M^2}\right). \tag{1.34}$$

Experimental value is $\Lambda = 213^{+38}_{-35}$ MeV [23] and demonstrates, that perturbative QCD cannot be used at low energy transfers. In fact, the running coupling constant $\alpha_S(-k^2)$ reaches value ~ 1 on momenta transfers $\sqrt{|k^2|} \sim 500$ MeV.

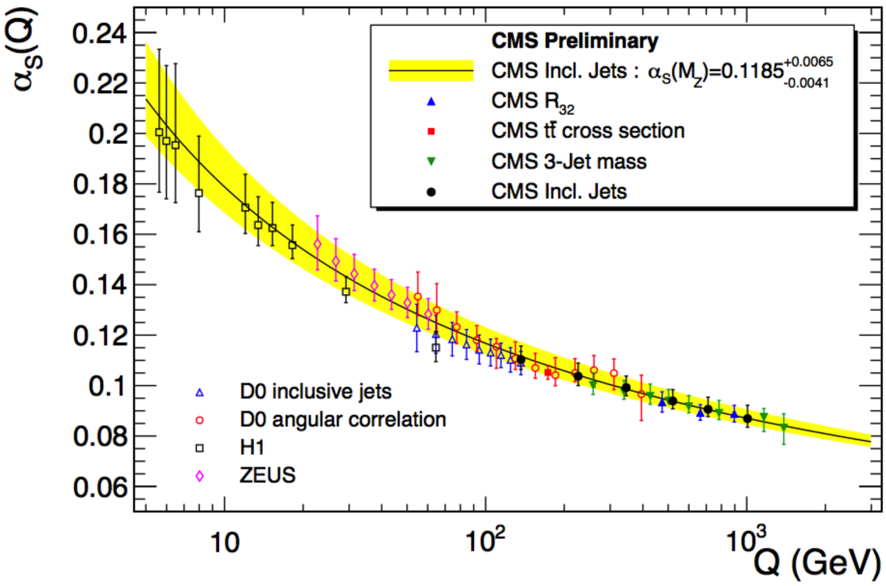

Figure 1.8: Experimental measurements of running coupling constant $\alpha_S(Q)$ (solid line) and its uncertainty (yellow band). $Q = \sqrt{|k^2|}$ in comparison to (1.33). Figure from [22].

The behaviour of coupling constant at low energy transfers is not explainable in the language of perturpative QCD just presented. It is non-perturbative effect known as the principle of color confinment, which states, that quarks when seperate, the gluon force field between them becomes stronger and its energy is consumed by the creation of quark anti-quark pair. This continues until there is no free color charge left. This principle forbids us from observing free quarks.

To understand e.g. structure of proton with rest mass $< 1\,\mathrm{GeV}$ it is clear non-perturbative QCD has to be used. The ideas of non-perturbative QCD will be introduced in next section.

1.5 Non-Perturbative QCD

The most well established non-perturbative approach to QCD is the lattice QCD (LQCD). In this section basic features of the LQCD will be presented. More informations on this extended topic can be found in [2, 24].

LQCD is QCD formulated on a hypercubic equally spaced lattice in space and time with lattice parameter a denoting the distance between neighboring sites. Quark fields are placed on sites whereas the gluon fields sit on the links between neighboring sites. From QCD it inherits the gauge invariance which has to be formulated on lattice structure. For $a \to 0$ action of LQCD coincides with that of QCD. LQCD contains 6 parameters - strong coupling constant and masses of 5 quarks (the top quark with lifetime $\sim 10^{-24}\,\mathrm{s}$ is not assumed by the theory).

Unlike perturbative expansion used in continuous QCD, numerical evaluation of the path integral defining LQCD allows non-perturbative calculations. Practical LQCD calculations are limited by the availability of computational resources and the efficiency of algorithms. LQCD suffers with both statistical and systematic errors, the former arising from the use of Monte-Carlo integration, the latter, e.g. from the use of non-zero values of a.

Present LQCD calculations are made on supercomputers like the QCDCQ supercomputer [25] with peak speed of 500 TFlops using lattice spacing $a \sim 0.05 - 0.15\,\mathrm{fm}$ in lattice volume $V \sim (2 - 6\,\mathrm{fm})^3$.

The Importance of LQCD lies in its ability to predict mass spectrum of observed mesons and baryons, including quark masses itself, and in investigation of topological structure of QCD vacuum. LQCD can be used to obtain PDFs (1.13) helping us to understand the structure of hadrons. Phenomenology of LQCD explains also the principle of color confinment.

Chapter 2

Experimental Framework

What we observe is not nature itself, but nature exposed to our method of questioning.

Werner Heisenberg

In the previous chapter, the key features of QCD - today's theory of strong interaction - were introduced. The predictions of QCD are tested at particle accelerators persistently and there is the whole army of theoretical physicists awaiting new discovery unexplainable in the terms of QCD. Unfortunately for them, there is no such measurement which would not be in agreement with QCD predictions up to date but the Large Hadron Collider can change this very soon.

In this chapter, the QCD will be raised from the theoretical description of the previous chapter, to the practical implementation on Large Hadron Collider, which will be described with emphasize on the ATALS detector. The all important concept of particle physics of hadron colliders - jet - will be introduced in this chapter.

2.1 The Large Hadron Collider and The ATLAS Detector

2.1.1 The Large Hadron Collider

The Large Hadron Collider (LHC) [26, 27] is a charged particle accelerator located on the border of France and Switzerland, near Geneva. Built using the areas of the Large Electron-Positron collider, the main accelerator ring, of a 27 km circumference, is located around 100 m below the surface. There are four main experiments located around the ring: A Large Ion Collider Experiment (ALICE), A Toroidal LHC ApparatuS (ATLAS), Compact Muon Solenoid (CMS) and Large Hadron Collider beauty (LHCb). The complete accelerator and detector system is shown at Figure 2.1.

LHC started to operate on November 23, 2009 and soon thereafter (March 30, 2010) the proton-proton collisions achieved the center-of-mass energy $\sqrt{s} = 7\,\text{TeV}$, which is

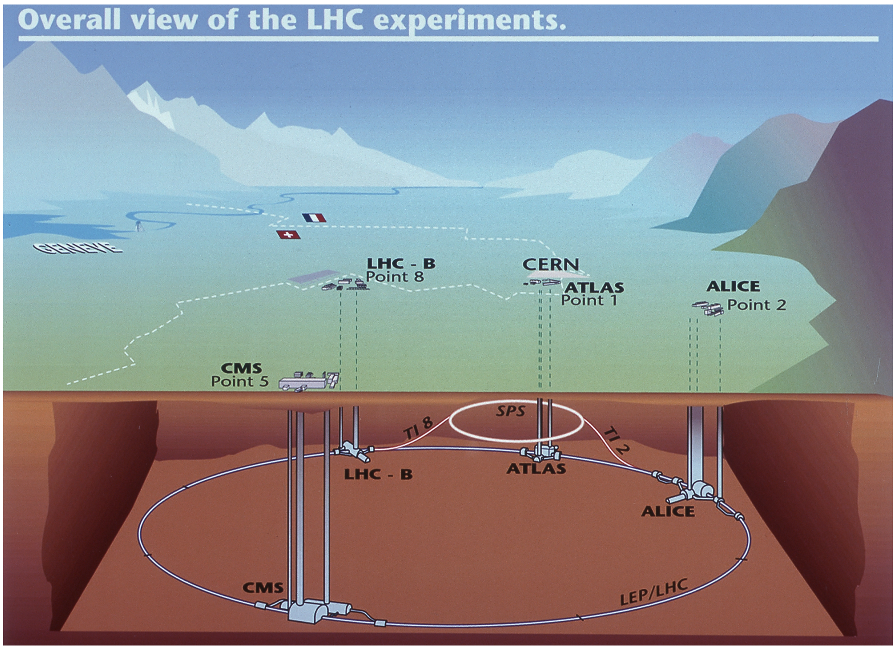

Figure 2.1: This diagram shows the locations of the four main experiments (ALICE, ATLAS, CMS and LHCb) that take place at the LHC. Located between 50 m and 150 m underground, huge caverns have been excavated to house the giant detectors. The Super Proton Synchotron (SPS), the final link in the pre-acceleration chain, and its connection tunnels to the LHC are also shown. Figure from [28]

halve of the design energy of the machine. On April 5, 2012, the machine started its successful $\sqrt{s} = 8\,\text{TeV}$ run.

Next to the proton-proton collisions first heavy-ion Pb-Pb collisions took place in 2010 at a center of mass energy per pair of colliding nucleons $\sqrt{s} = 2.76\,\text{TeV}$. Proton-Pb collisions at $\sqrt{s} = 5.02\,\text{TeV}$ occurring on LHC during 3 weeks of 2013 successfully demonstrated LHC capability to provide asymmetric collisions.

The first running period of the LHC, RunI, was very successful and resulted in important discoveries including Higgs boson on July 4, 2012 [29]. The accelerator complex has been upgraded including its experiments for two years and it is expected, the Run II will start in summer 2015 [30, 31]. In Run II the center-of-mass energy of proton-proton collisions will be raised up to $\sqrt{s} = 13\,\text{TeV}$ and beam crossing time will be reduced from the current 50 ns to 25 ns. Integrated luminosity in RunII will cross $100\,\text{fb}^{-1}$.

2.1.2 The ATLAS Detector

The ATLAS detector [32] is a general-purpose detector surrounding one of the interaction points of the LHC and with ~ 100 million of individual electronic channels it is the most complicated instrument ever created having one simple task: Record charged particle collisions up to the center-of-mass energy per pair of colliding nucleons $\sqrt{s} = 14\,\text{TeV}$. A detector overview is shown in Figure 2.2a, where the main sub-detector systems can be seen: the inner detector, used to reconstruct charged-particle tracks, the electromagnetic calorimeters, the hadronic calorimeters, and the muon spectrometer.

ATLAS uses a right-handed coordinate system with its origin at the interaction point in the center of the detector and the z axis along the beam pipe. The x axis points from the interaction point to the center of the LHC ring, and the y axis points upward. Cylindrical coordinates (r, ϕ) are used in the transverse plane, ϕ being the azimuthal angle around the beam pipe. Instead of polar angle θ pseudorapidity η is used throughout this thesis. For event selection the rapidity y plays an important role. In following definitions of pseudorapidity η and rapidity y, E stands for the total energy and p for size of total momentum:

$$\eta = -\frac{1}{2}\ln\left(\frac{p+p_z}{p-p_z}\right) = -\ln\left[\tan\left(\frac{\theta}{2}\right)\right], \quad (2.1)$$

$$y = -\frac{1}{2}\ln\left(\frac{E+p_z}{E-p_z}\right). \quad (2.2)$$

The transverse momentum p_T presents the component of momentum perpendicular to the beam line.

The main detector system relevant to this thesis is the ATLAS calorimeter, which is emphasized in Figure 2.2b. The calorimeter is divided into sub-detectors, providing overall coverage up to $|\eta| < 4.9$. The electromagnetic calorimeter, covering region $|\eta| < 3.2$, is a high-granularity sampling detector in which the active medium is liquid argon (LAr) interspaced with layers of lead absorber. The hadronic calorimeters are divided into three sections: a tile scintillator/steel calorimeter is used in both the barrel ($|\eta| < 1.0$) and extended barrel cylinders ($0.8 < |\eta| < 1.7$) while the hadronic endcap ($1.5 < |\eta| < 3.2$) consists of LAr/copper calorimeter modules. The forward calorimeter measures both electromagnetic and hadronic energy in the range $3.2 < |\eta| < 4.9$ using LAr/copper and LAr/tungsten modules.

2.2 Hadron Collision at LHC

In this section the phenomenological description of proton-proton collisions will be presented following picture in Figure 2.3 and Reference about Monte Carlo event generators [17].

Two incoming protons can be understood as the bag of partons. The collision alone is dominated by the interaction of two partons - one from each of the colliding hadrons. These partons are called incoming partons and the momentum transfer by their interaction is $Q \gg \Lambda$, so the perturbative QCD can be used in the process of hard scattering. Only a small fraction of collision energy has remained for the rest of the partons, which create the so called underlying event - particles, which do not come from the dominant QCD processes.

The perturbative QCD is used, while the remnants from collision of incoming partons are in distance $< 10^{-15}$ m from each other. There is for example enough time for top

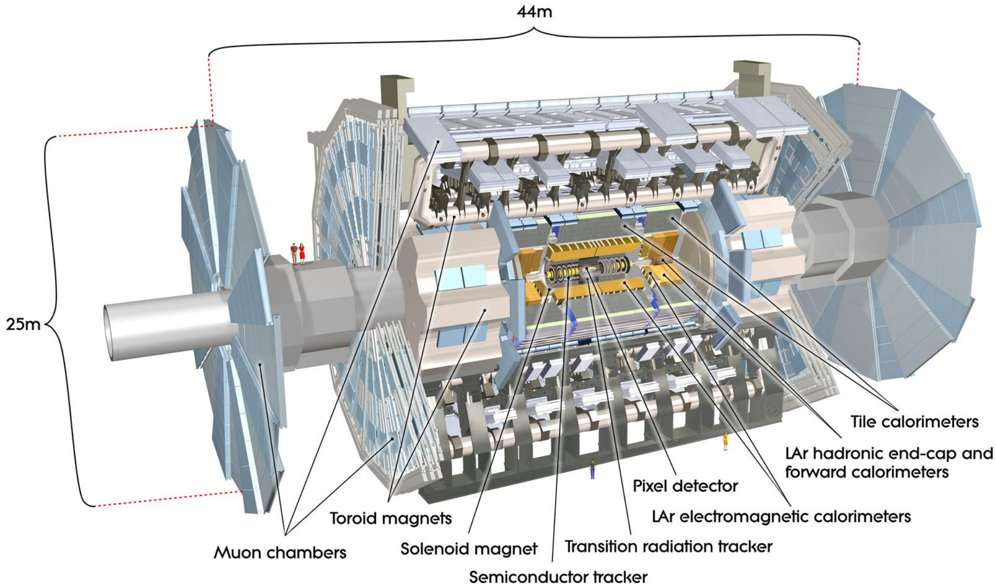

(a) ATLAS detector

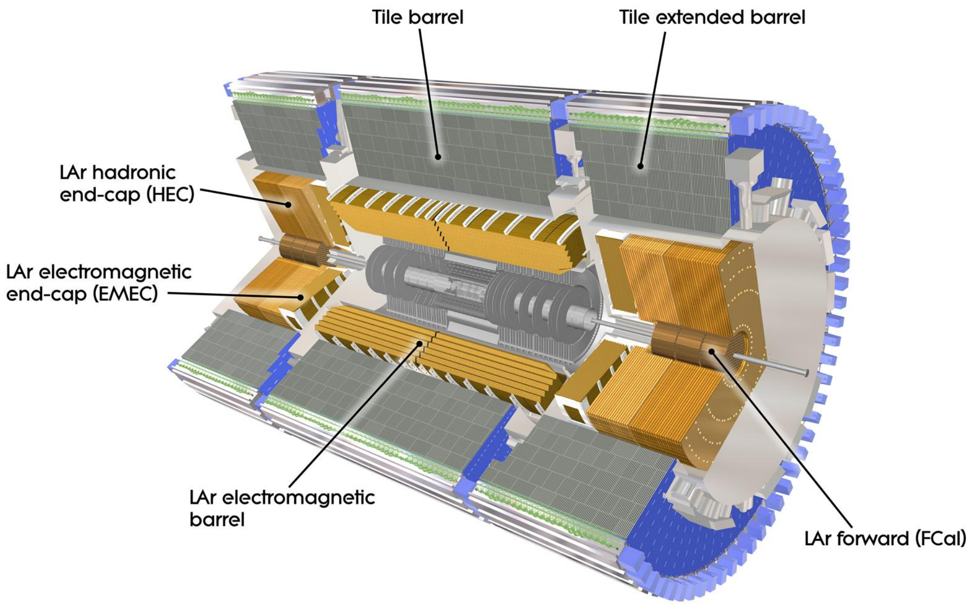

(b) Inner detector and calorimeter systems

Figure 2.2: (a) an overview of the ATLAS detector (b) detail on the inner detector and the calorimeters - the dominant sub-detector systems used in this thesis. Figures from [33].

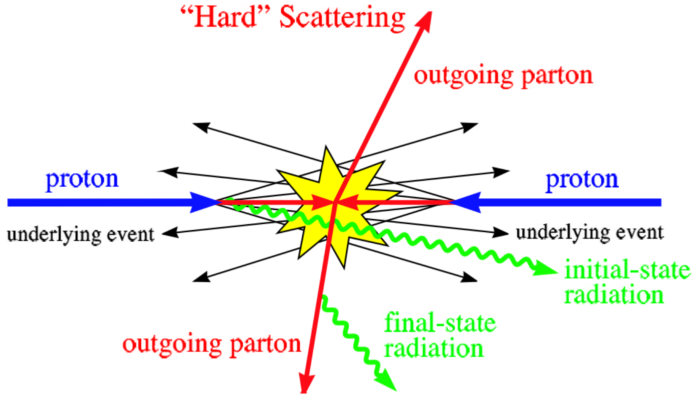

Figure 2.3: Schematic representation of a hard scattering proton-proton collision. Figure from [34]

quark to decay. When the distance between outgoing partons becomes greater, the non-perturbative QCD has to be used to describe the hadronisation - the process, by which a set of colored partons is transformed into a set of colorless primary hadrons which may then decay further.

During the collision, the electric and color charges of partons interact resulting in radiation of photons $q \to q\gamma$ and gluons $q \to qg$. These processes are described be perturbative QCD and lead to infrared and collinear divergences. However, infrared divergences can be canceled by Kinoshita–Lee–Nauenberg theorem [35,36], so only collinear divergences remain. There is no mechanism known up to date, which would solve the problem with collinear divergence. However, observables inclusive enough to be insensitive to processes that distinguish between different numbers of partons are not affected by infrared divergences. There is no possibility how to theoretically predict the energy of hardest outgoing particle, but it is possible to predict the energy flow in a cone from the point of scattering.

This is where the term jet comes to play. A jet can be naively seen as a group of collimated particles generated by the hadronisation of a parton in the scattering process and is the most important object used on hadron colliders for analysis of QCD processes.

2.3 Jet Algorithms

Jet algorithm is a generic "recipe" which takes a set of particles (or other objects with defined four-momenta) and returns jets created from them. That recipe usually involves a set of parameters which together with the recipe fully specify the jet definition. Following the remarks at the end of the previous section, jet algorithms should fulfill following conditions

1. Infrared safety - the presence of additional soft particles between two particles belonging to the same jet should not affect the recombination of these particles into a

jet.

2. Collinear safety - jet reconstruction should not depend on fact, if transverse momentum is carried by one particle, or if a particle is split into two collinear particles.

Principals of two jet algorithms are described here - fixed cone algorithm and k_t algorithm. First of these algorithms is more illustrative, the second one is used in ATLAS. Detailed description as well as other jet algorithms can be found in [37]. After definitions of jet algorithms it is shortly described, how the objects (not necessary particles) with defined four-momenta are constructed from the signal observed on the ATLAS detector.

2.3.1 Fixed cone algorithm

The first step of this algorithm is to order all input objects (reconstructed detector objects with four-momentum representation) in decreasing order in transverse momentum p_T. If the object with the highest p_T is above the seed threshold, all objects within a cone in pseudorapidity η and azimuth ϕ with $\Delta R = \sqrt{\Delta\eta^2 + \Delta\phi^2} < R_{cone}$, where R_{cone} is the fixed cone radius, are combined together. A new direction is calculated from the four-momenta inside the initial cone and a new cone is centered around it. Objects are then recollected in this new cone and again the direction is updated. This process continues until the direction of the cone does not change anymore after recombination, at which point the cone is considered stable and is called a jet. At this point, the next seed is taken from the input list and a new cone jet is formed with the same iterative procedure. This continues until no more seeds are available.

The jets found this way can share some constituents. This algorithm is both not infrared safe (Figure 2.4a) and not collinear safe (Figure 2.4b).

Parameters used by fixed cone algorithm are a seed threshold of $p_T > 1\,\mathrm{GeV}$, and a narrow ($R_{cone} = 0.4$) or a wide cone jet ($R_{cone} = 0.7$) option.

2.3.2 k_t algorithms

In this class of algorithms all pairs (i, j) of input objects are analyzed with respect to their relative transverse momentum squared, defined by

$$d_{ij} = \min\left(p_{T,i}^{2p}, p_{T,j}^{2p}\right)\frac{\Delta R_{ij}^2}{R^2} \tag{2.3}$$

and the squared p_T of object i relative to the beam axis

$$d_i = p_{T,i}^{2p}. \tag{2.4}$$

Here $\Delta R_{ij}^2 = (y_i - y_j)^2 + (\phi_i - \phi_j)^2$ and $p_{T,i}$, y_i and ϕ_i are respectively the transverse momentum, rapidity and azimuth of particle i. In addition to the radius parameter R, parameter p was added to split k_t algorithms into three categories.

- $p = 1$ k_t algorithm,
- $p = 0$ Cambridge/Aachen algorithm,
- $p = -1$ anti-k_t jet-clustering algorithm.

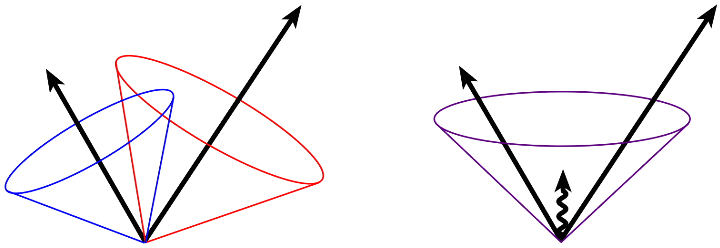

(a) Infrared unsafety

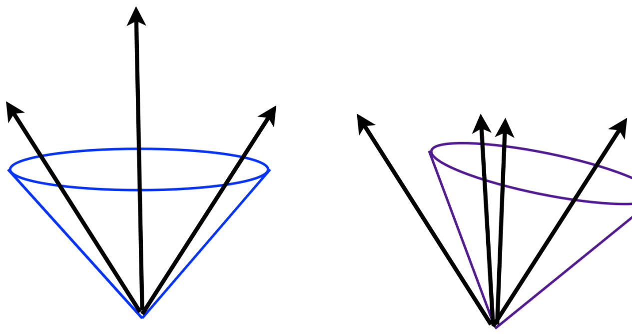

(b) Collinear unsafety

Figure 2.4: Illustration of (a) infrared unsafety and (b) collinear unsafety of fixed cone jet algorithm. Figures from [38].

The differences between these algorithms are detailed described in [39]. Recombination of calorimeter signal towers (see Section 2.3.3) in jets is for k_t and anti-k_t algorithms shown at Figure

These algorithms first find the minimum d_{min} of all d_{ij} and d_i. If d_{min} is in d_{ij}'s, the corresponding objects i and j are combined into a new object k using four-momentum recombination. Both objects i and j are removed from the list, and the new object k is added to it. If d_{min} is in d_i's, the object i is considered to be a jet by itself and removed from the list.

This means that all original input objects end up to be either part of a jet or to be jets by themselves. Contrary to the cone algorithm described earlier, no objects are shared between jets and the procedure is both infrared and collinear safe.

ATLAS uses anti-k_t algorithm with $R = 0.4$ for narrow and $R = 0.6$ for wide jets.

2.3.3 Calorimeter jets

The most important detectors for jet reconstruction are the ATLAS calorimeters. The ATLAS calorimeter system has about 200,000 individual cells of various sizes and with different readout technologies and cell geometries. For jet finding it is necessary to first combine these cell signals into larger signal object with physically meaningful four-momenta. The two concepts available are calorimeter signal towers and topological cell

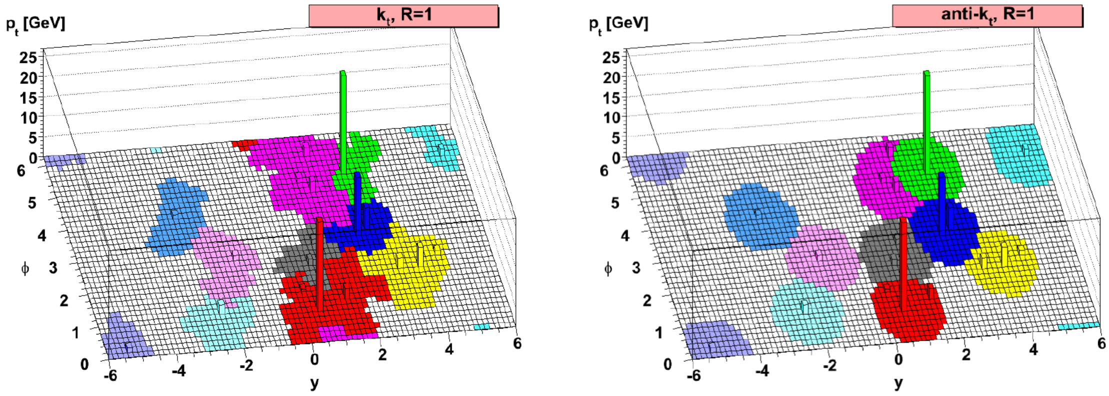

Figure 2.5: Illustration of k_t and anti-k_t jet algorithms with $R = 1$ for calorimeter signal towers in azimuth Φ and pseudorapidity y. Towers of the same color were recombined to one jet. Figure from [38]

clusters.

In the case of calorimeter signal towers, the cells are projected onto a fixed grid in pseudorapidity η and azimuth ϕ. The tower bin size is $\Delta\eta \times \Delta\phi = 0.1 \times 0.1$ in the whole acceptance region of the calorimeters, i.e. in $|\eta| < 5$ and $-\pi < \phi < \pi$ with approximately $100 \times 64 = 6,400$ towers in total.

The alternative representation of the calorimeter signals for jet reconstruction are topological cell clusters, which are basically an attempt to reconstruct three-dimensional "energy blobs" representing the showers developing for each particle entering the calorimeter. The clustering starts with seed cells with a signal-to-noise ratio, or signal significance $\Gamma = E_{cell}/\sigma_{noise,cell}$, above a certain threshold S, i.e. $|\Gamma| > S = 4$. All directly neighboring cells of these seed cells, in all three dimensions, are collected into the cluster. Neighbors of neighbors are considered for those added cells which have Γ above a certain secondary threshold N ($|\Gamma| > N = 2$). Finally, a ring of guard cells with signal significances above a basic threshold $|\Gamma| > P = 0$ is added to the cluster. After the initial clusters are formed, they are analyzed for local signal maximums by a splitting algorithm, and split between those maximums.

2.4 Jet corrections

Before jets can proceed to the data analysis, corrections have to be done to minimize detector effects including calorimeter non-compensation, noise, losses in dead material and cracks, longitudinal leakage and particle deflection in the magnetic field. Indispensable tool for jet corrections are Monte Carlo event generators - PYTHIA (?citace?) generating high-energy-physics events and GEANT4 (?citace?) or ATLFASTII (?citace?) detector simulations for simulating the detector response on PYTHIA generated events.

Using these tools it is possible to simulate jet reconstruction on three different stages of collisions indicated in Figure 2.6. First there are parton jets which are reconstructed

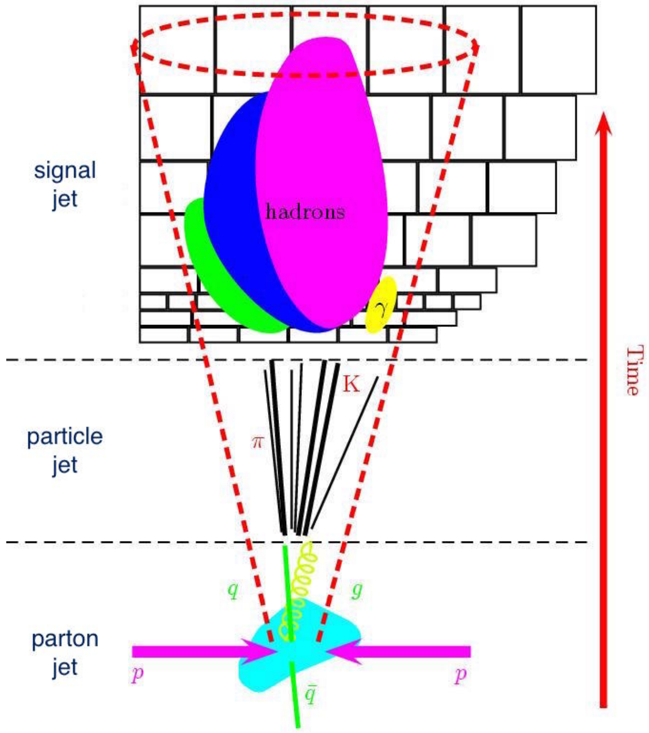

Figure 2.6: Possible levels of jet reconstructions. Figure from [40]

from the quarks, gluons and other elementary particles created just after the collision. Stable particles (with lifetime $c\tau \sim 10^{-15}$ m) created by hadronization are recombined into the particle jets. When collision reaches the detector, the detector simulation is used and the recorded signal is reconstructed into signal jets.

First the signal jets are corrected to the parton jets leading to modification of kinematic properties of signal jets in the process called calibration. Because the calibration is persistently evolving, each jet analysis uses as the input the uncalibrated signal jets which are then easily calibrated using standard library ApplyJetCalibration (?citace?).

There are some detector effects which are not removable by the calibration. These effects include the limited detector resolution (detector cells have finite dimensions) and the limited acceptance (not all events are recorded). The former leads to the smearing of jet kinematic properties wheres the later to lowering of observed cross section against the value theoretically predicted. Both of these effects are negatively influencing the observables and can be partially removed by the unfolding procedure, which unlike the jet calibration, is analysis dependent.

2.4.1 Unfolding

In this analysis, the distribution $f(p_T)$ of inclusive jet p_T is measured for $p_T \in \langle a, b \rangle$. Thanks to the detector imperfections, instead of physical variable p_T new variable x and its distribution $g(x)$ are measured. New distribution can be expressed as

$$g(x) = \int_a^b A(x, p_T) f(p_T) dx, \tag{2.5}$$

with the function $A(x, p_T)$ describing the detector response as can be seen when the detector is exposed to a particle beam with well known $p_T = p'_T$ meaning $f(p_T) = \delta(p_T - p'_T)$, leading to $g(x) = A(x, p'_T)$. The reconstruction of $f(p_T)$ from measured $g(x)$ is called unfolding.

For practical purposes the equation (2.5) should be discretized so instead of continuous distribution $g(x)$ the discretized values $g_i = \int_{N(i)} g(x)dx$ of discretized observable $f_i = \int_{N(i)} f(p_T)dp_T$ are measured, where the integral goes over measurable $N(i) \subset \langle a, b \rangle$. For simplicity assume $x \in \langle a, b \rangle$ is discretized in the same way as the physical p_T. Equation (2.5) then reads

$$g = Af, \tag{2.6}$$

with g and f being vectors of g_i's and f_i's respectively and A matrix derived from $A(x, p_T)$. If the limited acceptance would be the only detector problem, then A would be diagonal matrix with some elements < 1. When the limited resolution comes to play, the diagonal entries starts to smear out of the diagonal and the matrix A starts to complicate.

The unfolding result which offers the solution of (2.6) by inversion of matrix A is mostly disappointing as is illustrated e.g. in (?citace?). For result improvement, different unfolding methods were developed including iterative Bayesian (?citace?), Singular Value Decomposition (?citace?), or iterative, dynamically stabilized (IDS) method (?citace?), which is the method used in this thesis.

Chapter 3

Data Analysis

In physics, you don't have to go around making trouble for yourself - nature does it for you.

Frank Wilczek

QCD jets are the most common hard objects observed at hadron colliders, with their cross section exceeding any other physics process by orders of magnitude. Measurement of inclusive jet cross section thus provide the first test for both QCD predictions and the detector performance. LHC Run II should open new kinematic region with expectation of observation of jets with p_T in TeV region.

This chapter describes the details of the inclusive jet cross section analysis.

3.1 Data Characteristics

Data used in this thesis are Monte Carlo generated events of pp collisions at the center-of-mass energy $\sqrt{s} = 13\,\text{TeV}$ by PYTHIA8 (?citace?) event generator using CT10 PDFs (?citace?) and ATLAS underlying event tune AU2 (?citace?). PYTHIA8 performs LO QCD calculations. The response of the ATLAS detector on these events was calculated with ?GEANT4? (?citace?) software toolkit.

Particles were recombined using anti-k_t jet algorithm with parameter $R = 0.4$. There are parton jets reconstructed from the PYTHIA8 output, which further in this thesis are denoted truth jets, and next to them, there are the signal jets reconstructed from the output of GEANT4 detector simulation as the topological cell clusters.

Generated events are divided into JZXW samples according to the leading truth jet p_T. These samples differ in event weight which is for the whole event calculated as the product of cross section, filter efficiency, inverse number of events and additional weight factor which is for each event stored in `EventInfoAux` container. Values used in this thesis are given in Table 3.1.

JZXW	p_T range (GeV)	Cross-section (fb)	Filter Efficiency	# envents
JZ0W	0 - 20	7.8420e+13	9.7193e-01	3498000
JZ1W	20 - 80	7.8420e+13	2.7903e-04	2998000
JZ2W	80 - 200	5.7312e+10	5.2261e-03	500000
JZ3W	200 - 500	1.4478e+09	1.8068e-03	499500
JZ4W	500 - 1000	2.3093e+07	1.3276e-03	477000
JZ5W	1000 - 1500	2.3793e+05	5.0449e-03	499000
JZ6W	1500 - 2000	5.4279e+03	1.3886e-02	493500
JZ7W	2000 +	9.4172e+02	6.7141e-02	497000

Table 3.1: The cross-sections, filter efficiency and number of events for the JZXW samples which differ in the leading truth jet p_T.

Analysis uses jets with transverse momentum $p_T > 15\,\text{GeV}$ and rapidity $|y| < 4$ and is done in p_T and $|y|$ bins with the following edges

$$\begin{aligned} p_T =& 15 : 20 : 25 : 35 : 45 : 55 : 70 : 85 : 100 : 116 : 134 : 152 : 172 : 194 : 216 : 240 : 264 : 290 : \\ & 318 : 346 : 376 : 408 : 442 : 478 : 516 : 556 : 598 : 642 : 688 : 736 : 786 : 838 : 894 : 952 : \\ & 1012 : 1076 : 1162 : 1310 : 1530 : 1992 : 2300 : 2800 : 3400 : 4100 : 5000 : 6000 : 7200\,\text{GeV} \\ |y| =& 0.0 : 0.5 : 1.0 : 1.5 : 2.0 : 2.5 : 3.0 : 3.5 : 4.0 \end{aligned} \tag{3.1}$$

3.2 Event Selection

Signal jets were calibrated using ApplyJetCalibration library version 3.28 and configuration parameters were loaded from the `JES_Full2012dataset_May2014.config` with calibration sequence `JetArea_Residual_EtaJES`. In next signal jets denotes the signal calibrated jets.

In this section the jet selection criteria and matching of truth with signal jets are described. The former is needed to cut those jets off, which were misinterpreted by the detector, by the later the inputs for the unfolding procedure are obtained. Description of the unfolding procedure will follow in the next section.

3.2.1 Jet Cuts

- **$\mathbf{p_T}$ Cut**

  something something something

- **y Cut**

  something something something

- **Zero jet (0jet) Cut**

  something something something

- **Leading Ration (LR) Cut**

  something something something

Discuss results of cutting. 3.1 3.2

3.2.2 Jet Matching

Describe matching procedure. Discuss results of matching. matchedSignal, unmatchedSignal, matchedTruth, unmatchedTruth. 3.2 3.2

3.3 Unfolding

The main ingredient for the unfolding procedure is the transfer matrix Aij, which is derived from Monte Carlo and contains the number of jets that have been reconstructed in bin i with a matched truth jet that was generated in bin j. A reconstructed and true jet are considered matched if their centers lie within DeltaR $<$0.3 of each other, and the matching is unique. The transfer matrix does not include unmatched jets, so an equivalent fraction of jets in data needs to be removed from the unfolding procedure: a multiplicative inefficiency equal to the fraction of unmatched jets is applied to data before the start of the unfolding procedure, and the equivalent number of jets is restored after the unfolding.

How the unfolding matrix is filled. MatchingEfficiency for signal and truth jets. IDSUnfolding

The unfolding procedure for the inclusive jet measurement is iterated once.

3.4 Comparison with Prediction

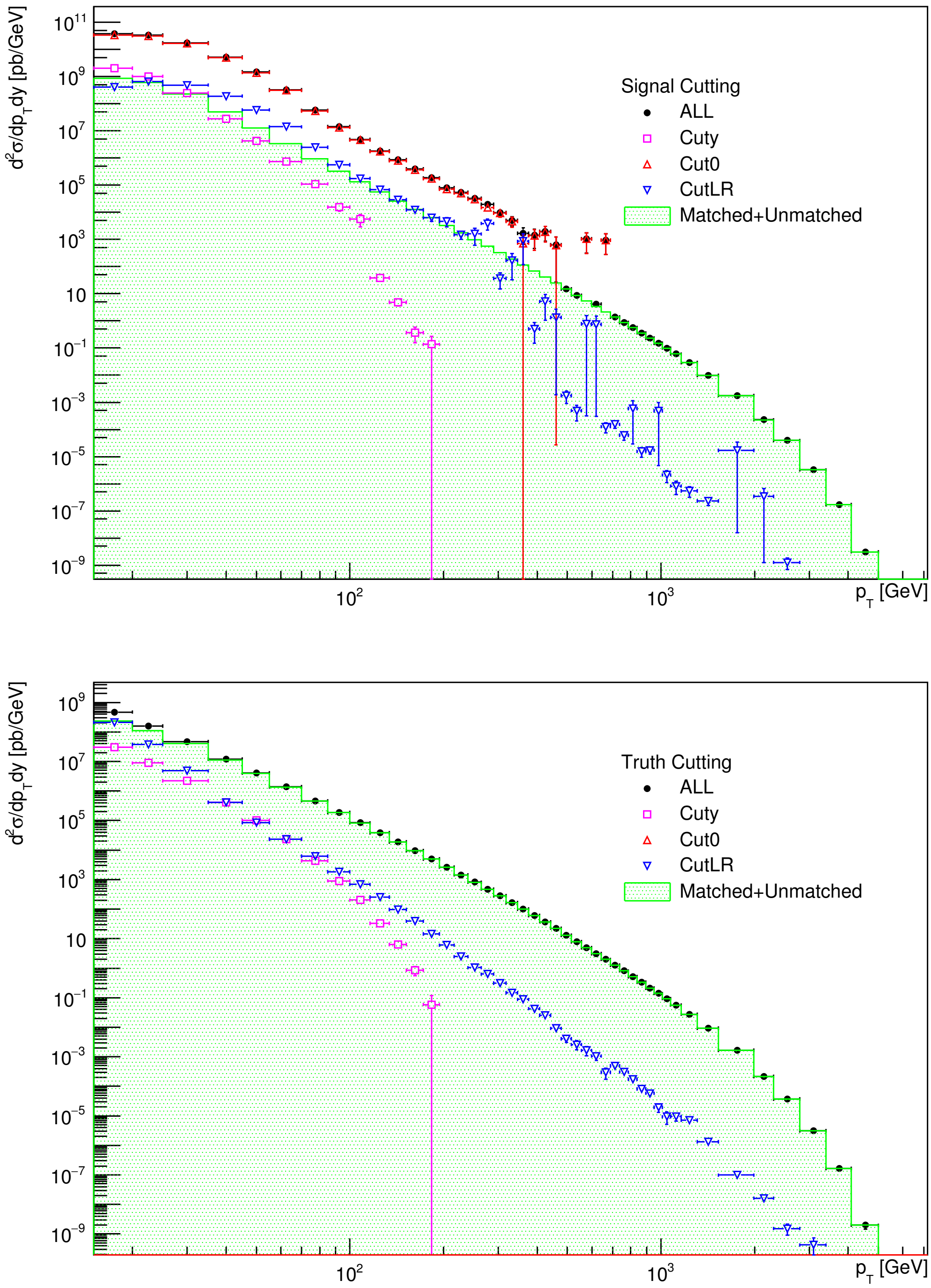

Figure 3.1: Cutting

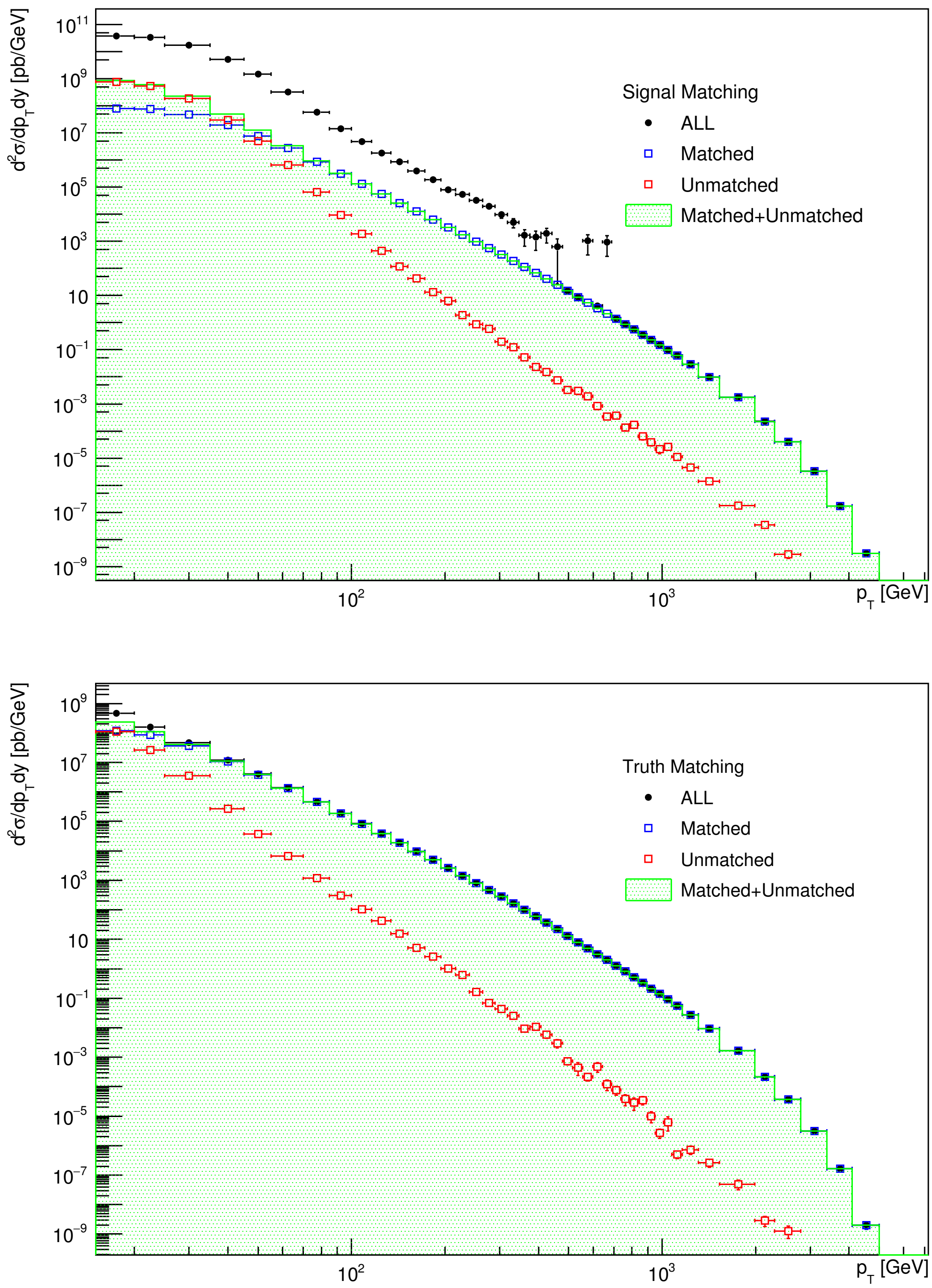

Figure 3.2: Matching

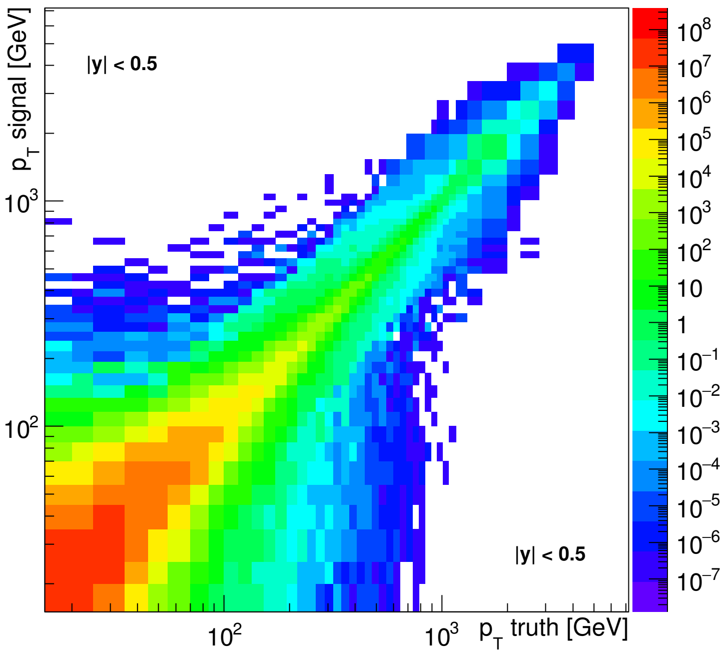

Figure 3.3: Unfolding matrix detail

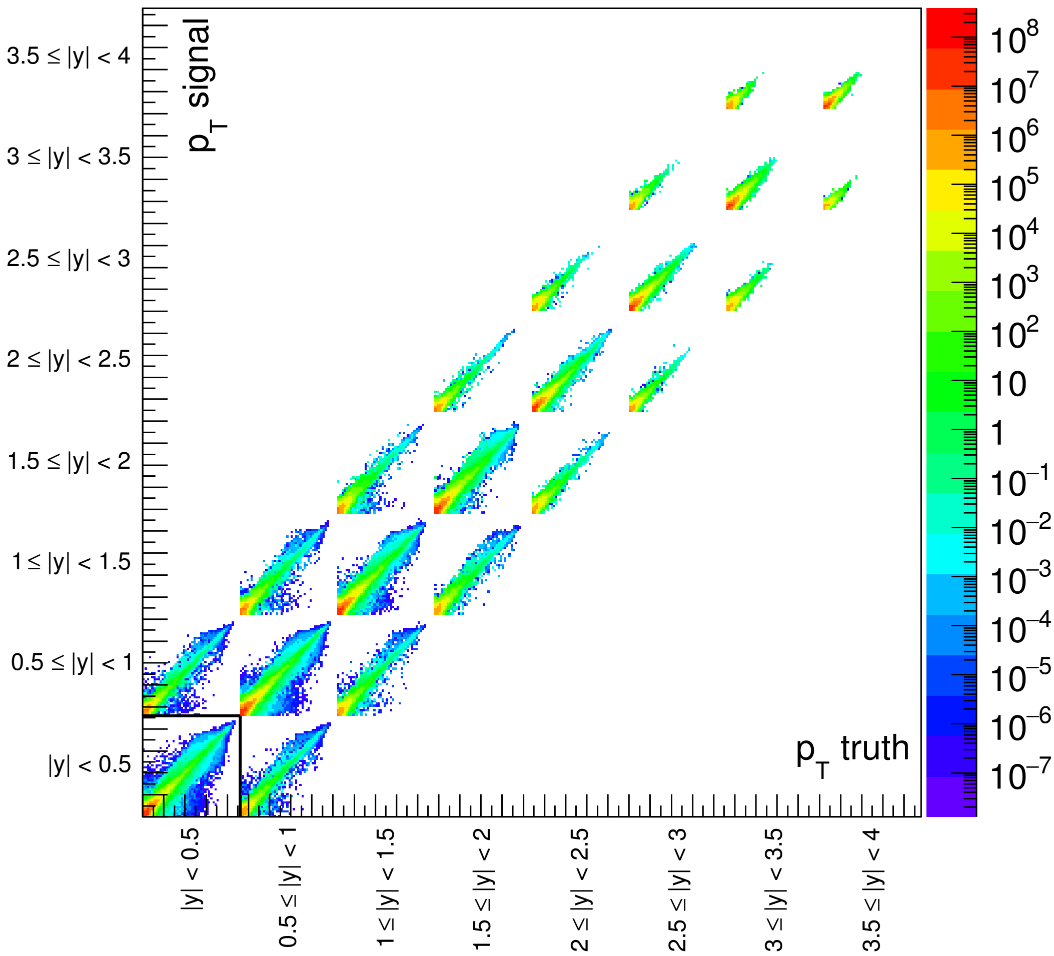

Figure 3.4: Unfolding matrix all

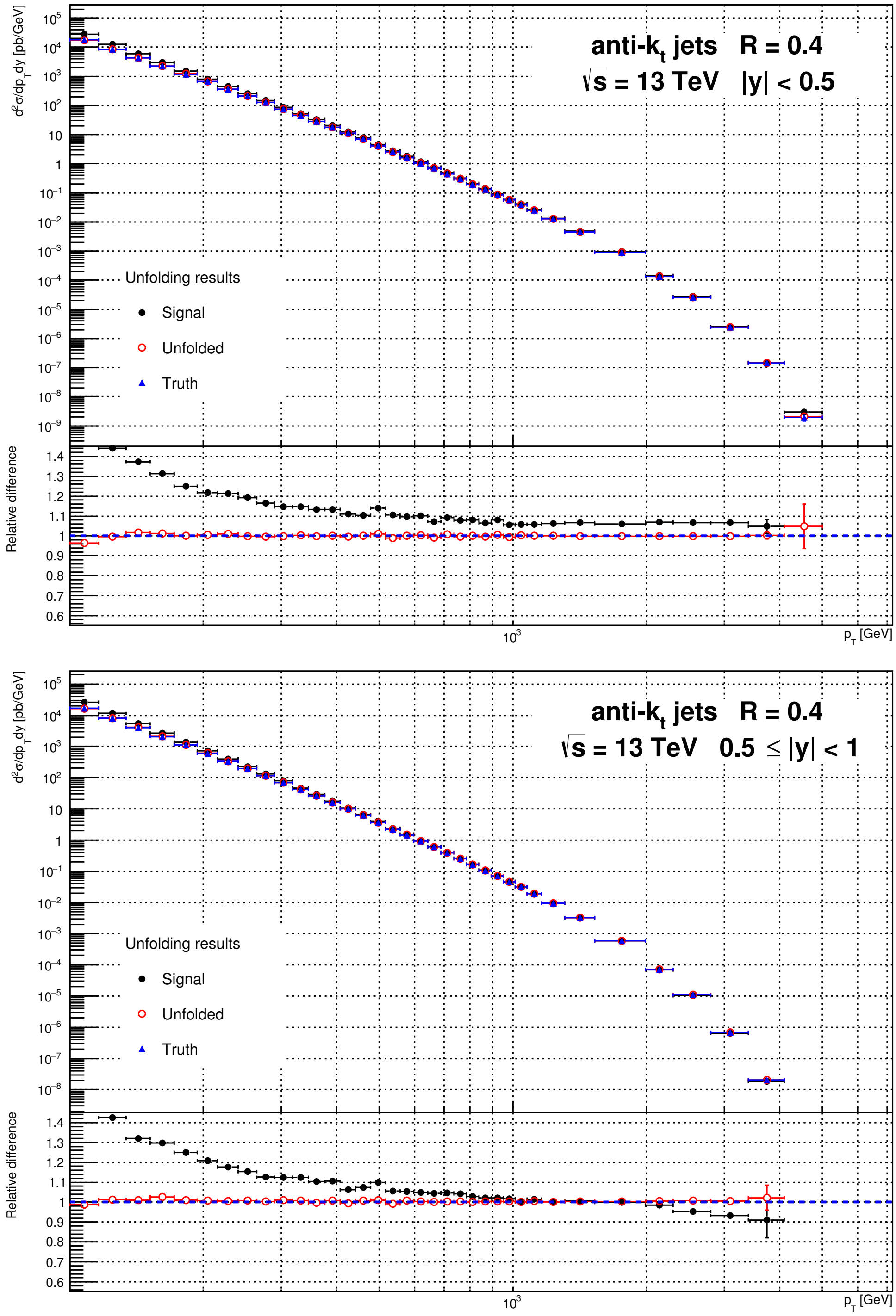

Figure 3.5: Unfolding1

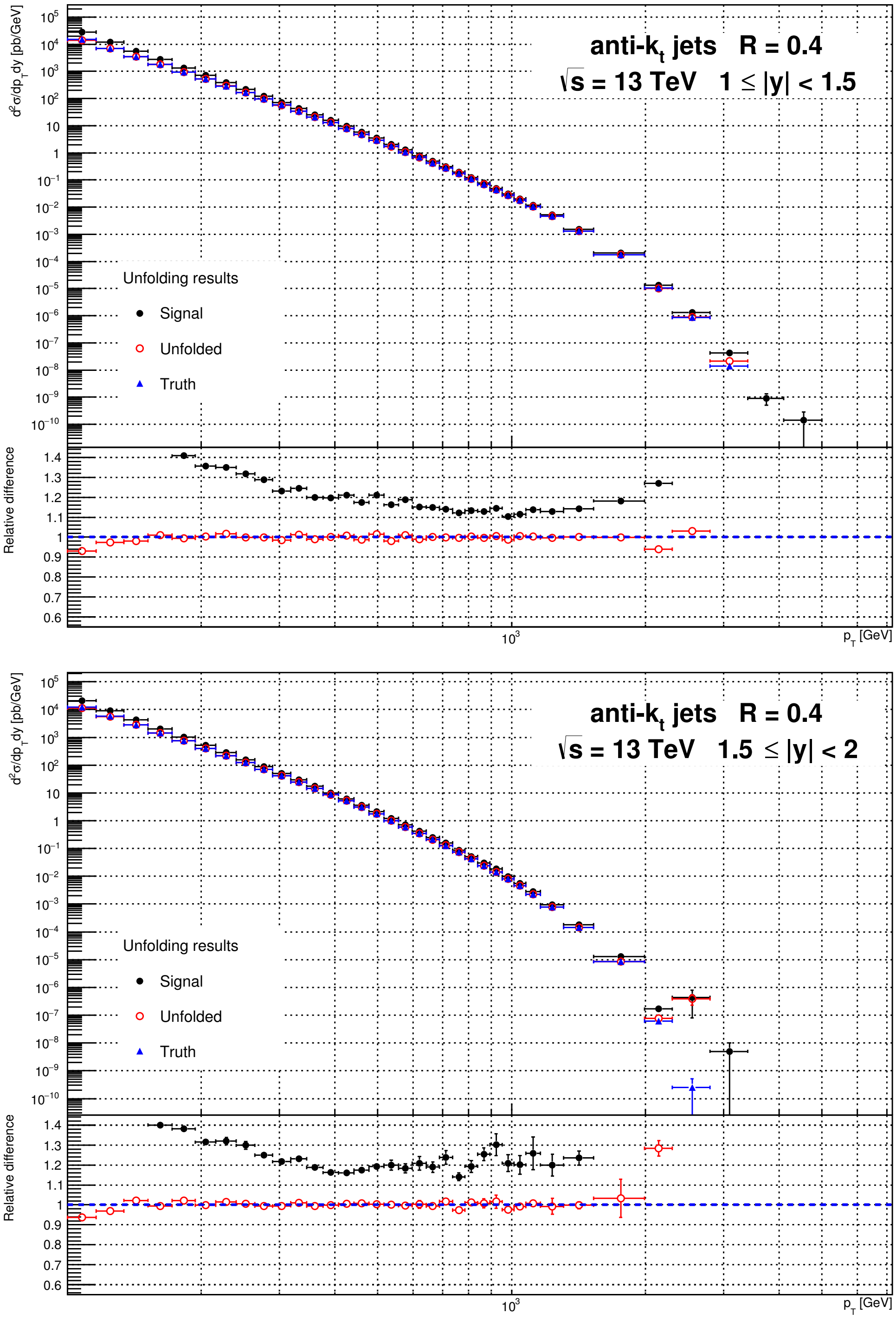

Figure 3.6: Unfolding2

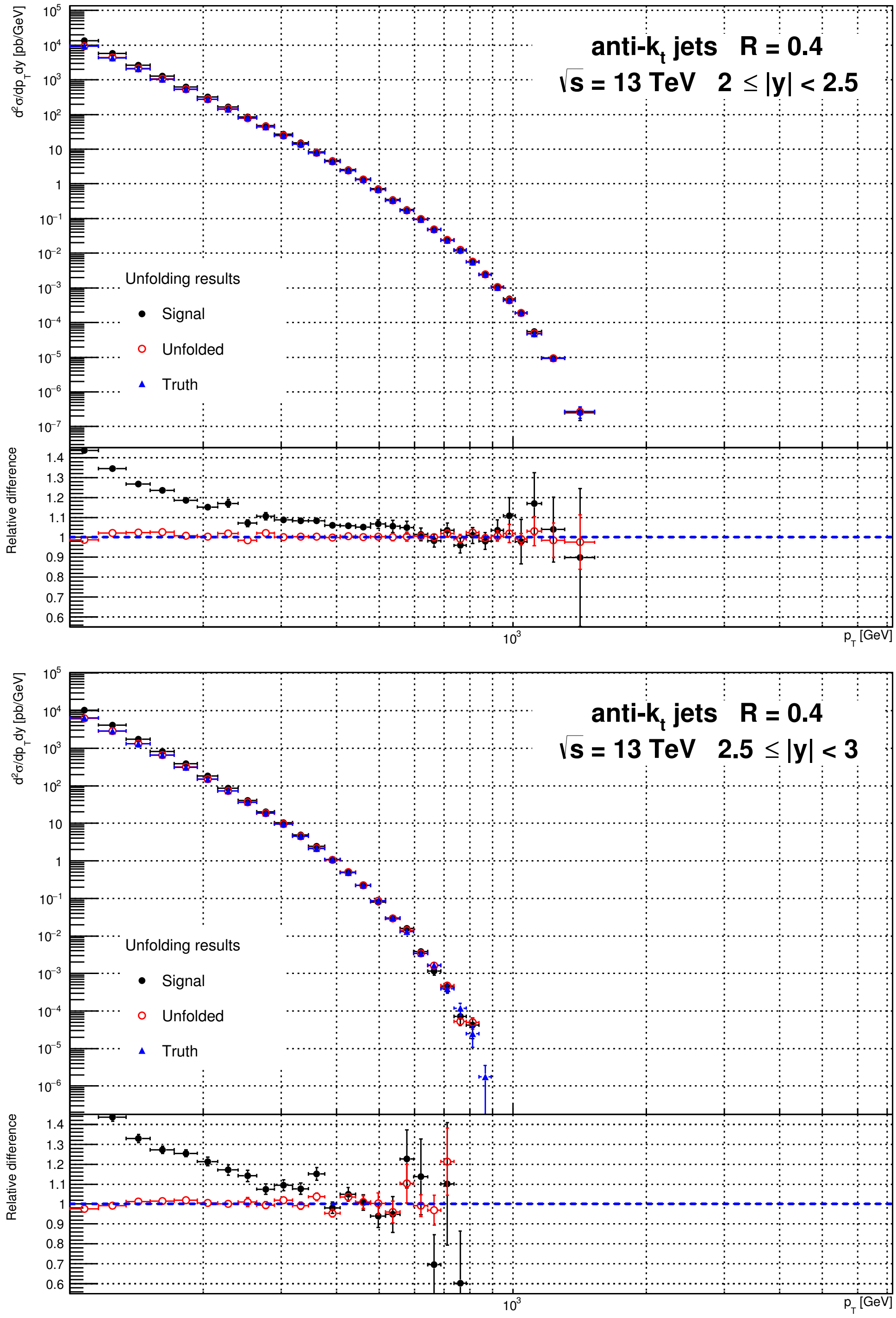

Figure 3.7: Unfolding3

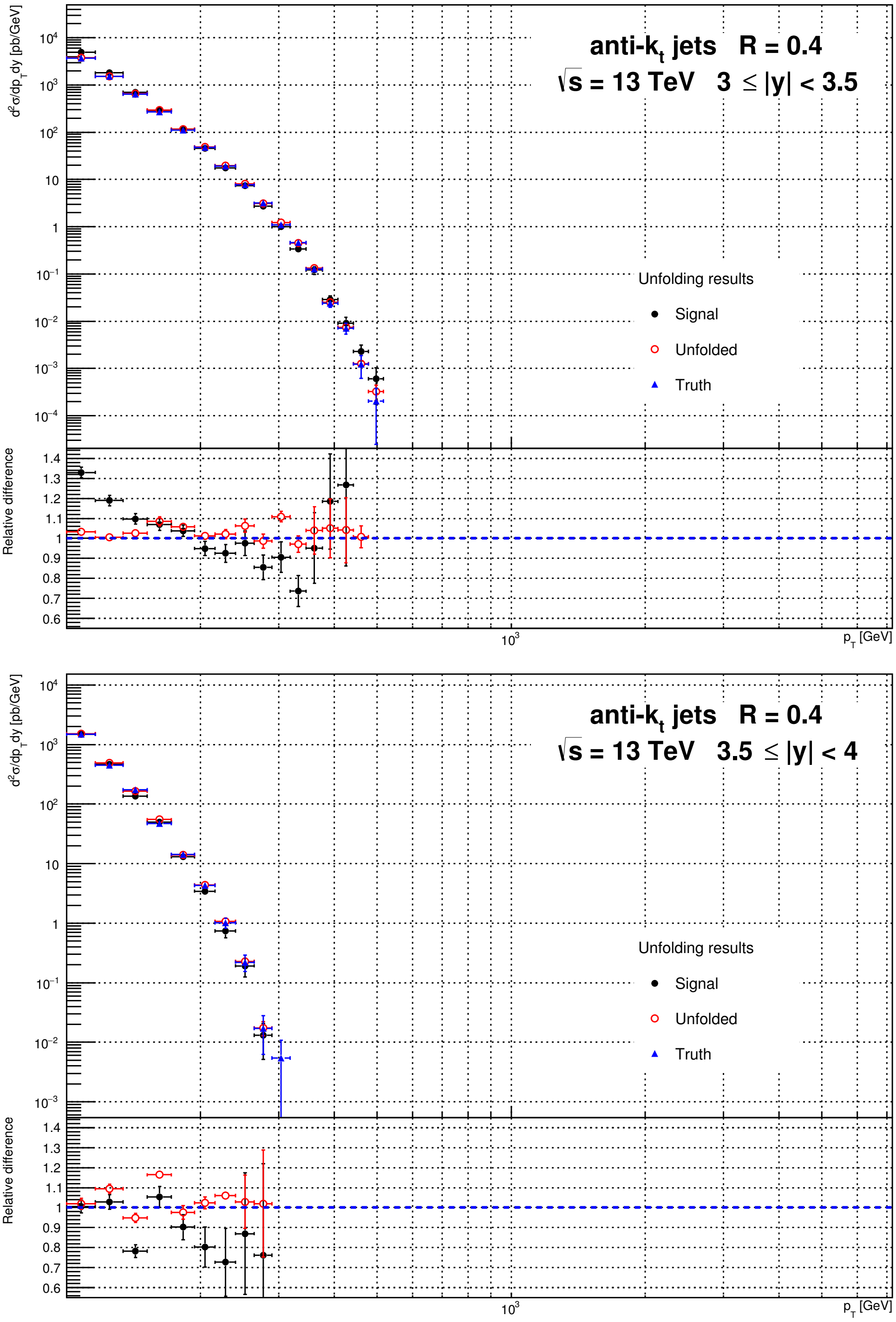

Figure 3.8: Unfolding4

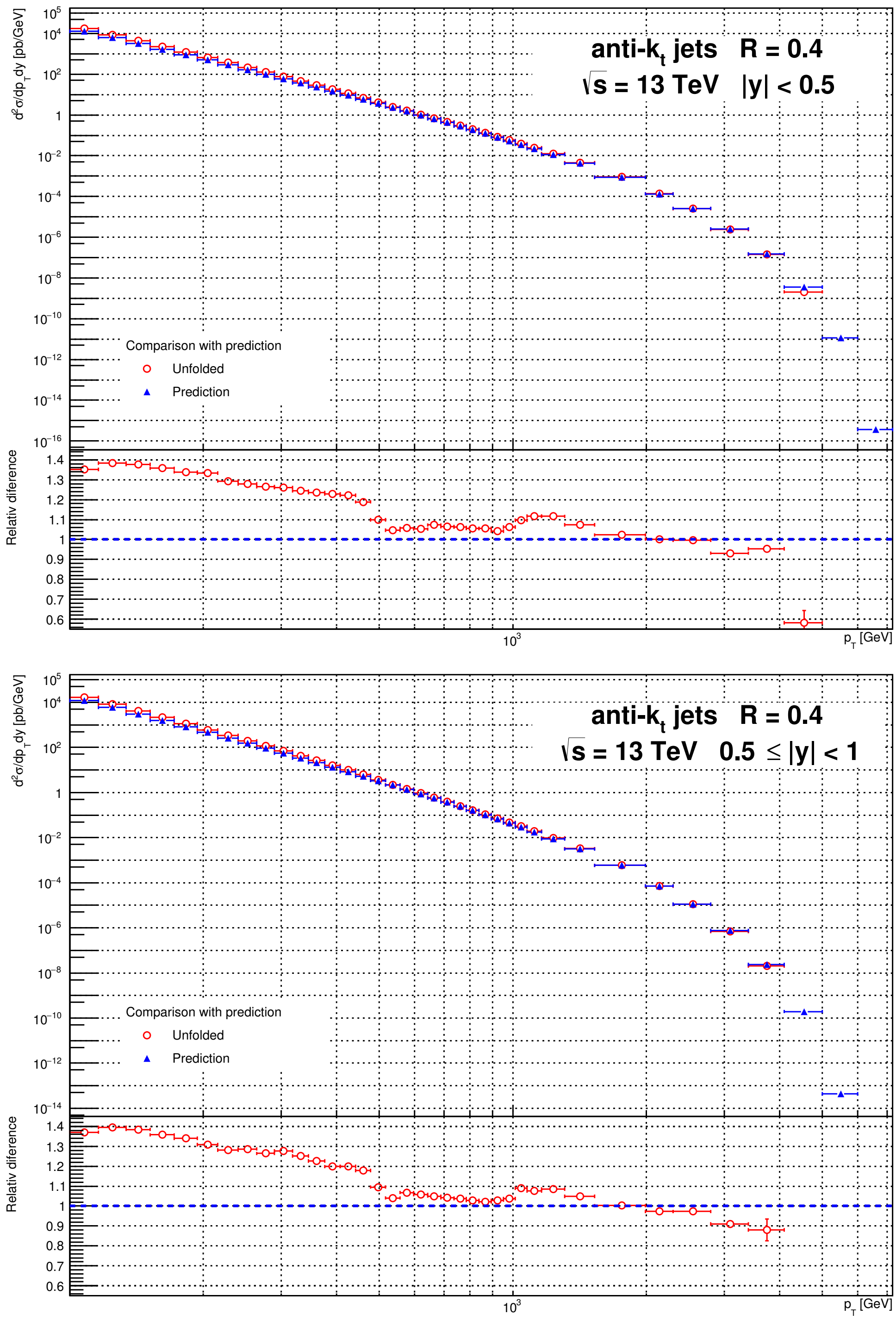

Figure 3.9: Comparision unfolding with prediction 1

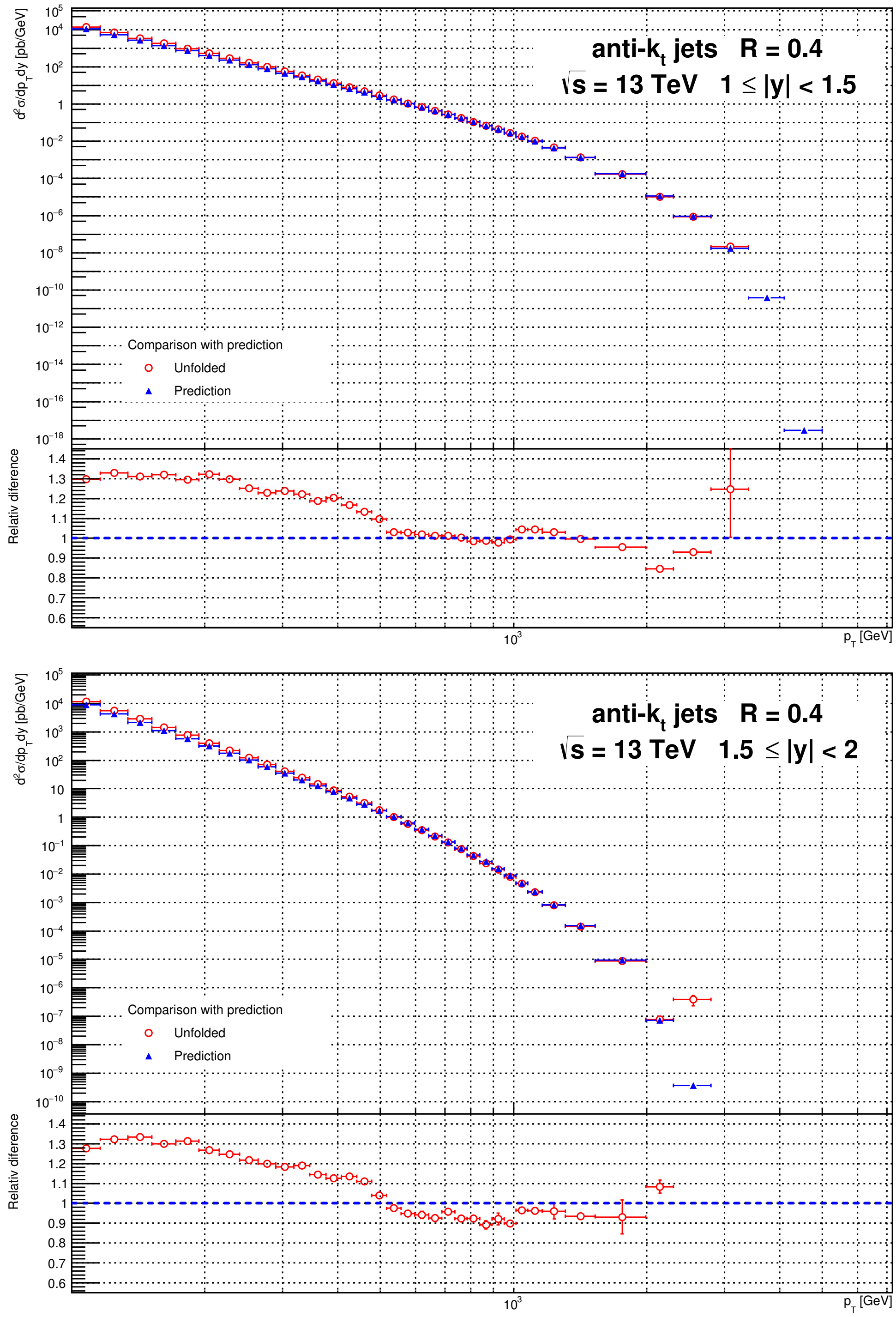

Figure 3.10: Comparision unfolding with prediction 2

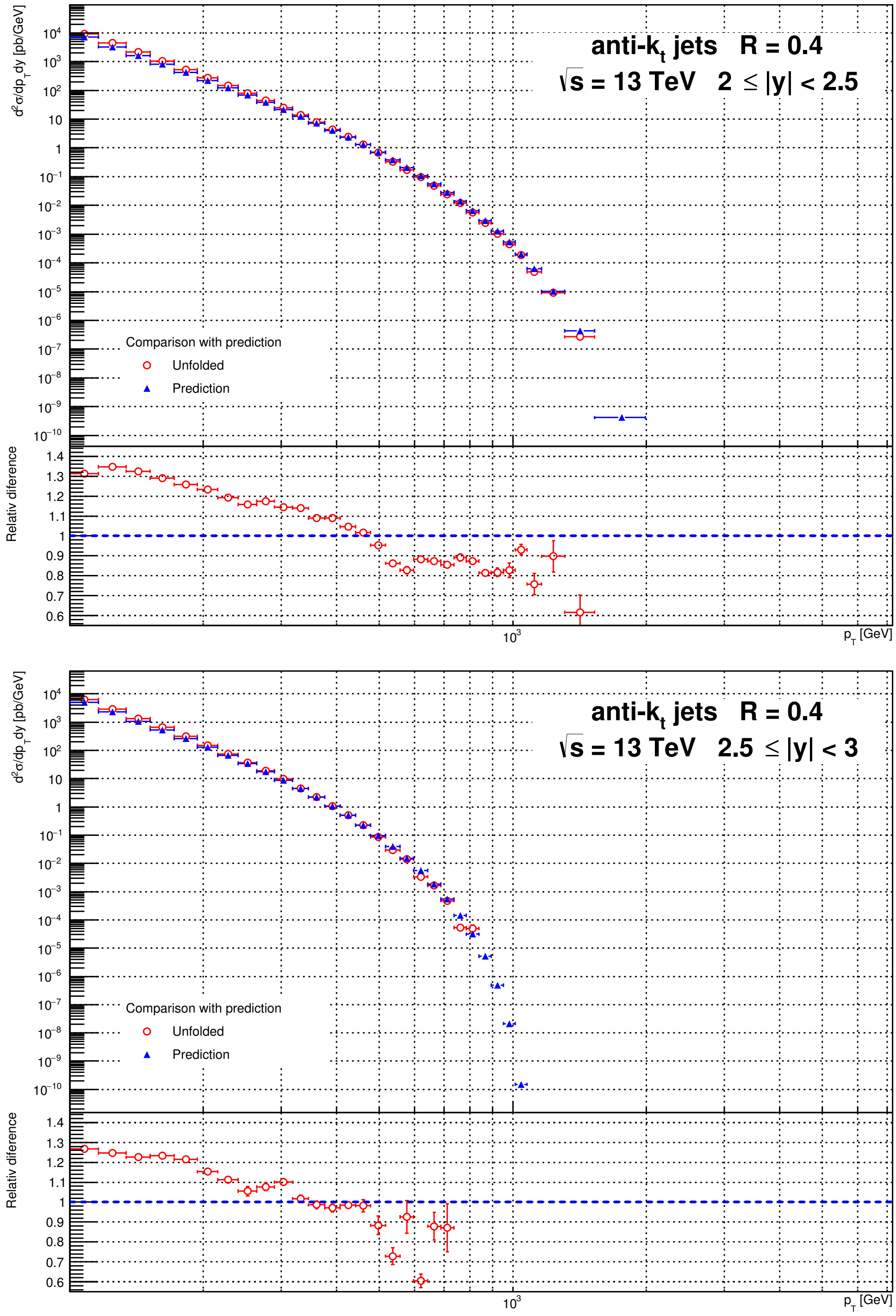

Figure 3.11: Comparision unfolding with prediction 3

# jets		**ALL**	JZ0W	JZ1W	JZ2W	JZ3W	JZ4W	JZ5W	JZ6W	JZ7W
Signal		**1.10e+08**	3.22e+07	3.59e+07	6.67e+06	7.07e+06	6.28e+06	7.29e+06	7.13e+06	7.11e+06
Truth		**7.22e+07**	3.15e+06	3.00e+07	6.17e+06	6.91e+06	6.20e+06	6.98e+06	6.53e+06	6.25e+06
CutPt	Signal	**1.32e+07** **12.1 %**	5.45e+06 17.0 %	4.38e+06 12.2 %	6.50e+05 9.7 %	5.87e+05 8.3 %	4.76e+05 7.6 %	5.48e+05 7.5 %	5.52e+05 7.7 %	5.63e+05 7.9 %
	Truth	**4.67e+07** **64.7 %**	3.11e+06 98.7 %	2.20e+07 73.1 %	3.86e+06 62.6 %	4.00e+06 57.8 %	3.42e+06 55.1 %	3.74e+06 53.6 %	3.43e+06 52.5 %	3.23e+06 51.6 %
Cuty	Signal	**2.46e+06** **2.2 %**	8.02e+05 2.5 %	9.54e+05 2.7 %	1.42e+05 2.1 %	1.28e+05 1.8 %	1.03e+05 1.6 %	1.16e+05 1.6 %	1.10e+05 1.5 %	1.08e+05 1.5 %
	Truth	**5.03e+05** **0.7 %**	3.14e+03 0.1 %	3.19e+05 1.1 %	4.54e+04 0.7 %	3.79e+04 0.5 %	2.88e+04 0.5 %	2.78e+04 0.4 %	2.22e+04 0.3 %	1.83e+04 0.3 %
Cut0jet	Signal	**2.62e+07** **23.9 %**	2.56e+07 79.6 %	5.49e+05 1.5 %	0.00e+00 0.0 %	0.00e+00 0.0 %	0.00e+00 0.0 %	0.00e+00 0.0 %	0.00e+00 0.0 %	0.00e+00 0.0 %
	Truth	**0.00e+00** **0.0 %**	0.00e+00 0.0 %	0.00e+00 0.0 %	0.00e+00 0.0 %	0.00e+00 0.0 %	0.00e+00 0.0 %	0.00e+00 0.0 %	0.00e+00 0.0 %	0.00e+00 0.0 %
CutLR	Signal	**3.64e+06** **3.3 %**	2.27e+05 0.7 %	3.37e+06 9.4 %	2.99e+04 0.4 %	7.07e+03 0.1 %	2.33e+03 0.0 %	1.63e+03 0.0 %	7.14e+02 0.0 %	6.31e+02 0.0 %
	Truth	**5.21e+05** **0.7 %**	2.15e+04 0.7 %	4.74e+05 1.6 %	1.82e+04 0.3 %	4.45e+03 0.1 %	1.33e+03 0.0 %	9.03e+02 0.0 %	4.37e+02 0.0 %	2.78e+02 0.0 %
Matched	Signal	**2.13e+07** **19.5 %**	7.95e+03 0.0 %	5.99e+06 16.7 %	1.95e+06 29.3 %	2.54e+06 36.0 %	2.46e+06 39.1 %	2.88e+06 39.5 %	2.78e+06 38.9 %	2.72e+06 38.2 %
	Truth	**2.13e+07** **29.5 %**	7.95e+03 0.3 %	5.99e+06 19.9 %	1.95e+06 31.7 %	2.54e+06 36.8 %	2.46e+06 39.6 %	2.88e+06 41.3 %	2.78e+06 42.5 %	2.72e+06 43.5 %
Unmatched	Signal	**4.28e+07** **39.0 %**	6.15e+04 0.2 %	2.06e+07 57.5 %	3.89e+06 58.4 %	3.81e+06 53.8 %	3.24e+06 51.6 %	3.75e+06 51.4 %	3.69e+06 51.8 %	3.72e+06 52.3 %
	Truth	**3.14e+06** **4.4 %**	7.51e+03 0.2 %	1.30e+06 4.3 %	2.89e+05 4.7 %	3.29e+05 4.8 %	2.95e+05 4.8 %	3.29e+05 4.7 %	3.03e+05 4.6 %	2.88e+05 4.6 %

Table 3.2: Cut and matching efficiency.

Conclusion

List of Figures

List of Tables

Bibliography

[1] "Standard model — Wikipedia, the free encyclopedia." http://en.wikipedia.org/wiki/Standard_Model, 2015.

[2] W. Greiner, D. Bromley, S. Schramm, and E. Stein, *Quantum Chromodynamics.* Springer, 2007.

[3] J. Horejsi, *Fundamentals of Electroweak Theory.* Karolinum Press, 2002.

[4] D. Griffiths, *Introduction to Elementary Particles.* Physics textbook, Wiley, 2008.

[5] W. Cottingham and D. Greenwood, *An Introduction to the Standard Model of Particle Physics.* Cambridge University Press, 2007.

[6] T. Nakano and K. Nishijima, "Charge independence for v-particles," *Progress of Theoretical Physics*, vol. 10, no. 5, pp. 581–582, 1953.

[7] M. Gell-Mann, "The interpretation of the new particles as displaced charge multiplets," *Il Nuovo Cimento*, vol. 4, no. 2, pp. 848–866, 1956.

[8] M. Gell-Mann and Y. Ne'eman, *The eightfold way.* Frontiers in Physics, New York, NY: Benjamin, 1964.

[9] G. Zweig, "An SU_3 model for strong interaction symmetry and its breaking; Version 2," p. 80 p, Feb 1964.

[10] H. Georgi, *Lie Algebras in Particle Physics: From Isospin to Unified Theories.* Frontiers in Physics Series, Westview Press, 1999.

[11] "Eightfold way — Wikipedia, the free encyclopedia." http://de.wikipedia.org/wiki/Eightfold_Way, 2015.

[12] M. Gell-Mann and H. Fritzsch, *Murray Gell-Mann: selected papers.* World Scientific series in 20th century physics, Singapore: World Scientific, 2010.

[13] S. Okubo, "Note on unitary symmetry in strong interactions," *Progress of Theoretical Physics*, vol. 27, no. 5, pp. 949–966, 1962.

[14] S. L. Glashow, J. Iliopoulos, and L. Maiani, "Weak interactions with lepton-hadron symmetry," *Phys. Rev. D*, vol. 2, pp. 1285–1292, Oct 1970.

[15] M. Kobayashi and T. Maskawa, "Cp-violation in the renormalizable theory of weak interaction," *Progress of Theoretical Physics*, vol. 49, no. 2, pp. 652–657, 1973.

[16] E. D. Bloom, D. H. Coward, H. DeStaebler, J. Drees, G. Miller, L. W. Mo, R. E. Taylor, M. Breidenbach, J. I. Friedman, G. C. Hartmann, and H. W. Kendall, "High-energy inelastic $e-p$ scattering at 6° and 10°," *Phys. Rev. Lett.*, vol. 23, pp. 930–934, Oct 1969.

[17] K. Olive *et al.*, "Review of Particle Physics," *Chin.Phys.*, vol. C38, p. 090001, 2014.

[18] C. N. Yang and R. L. Mills, "Conservation of isotopic spin and isotopic gauge invariance," *Phys. Rev.*, vol. 96, pp. 191–195, 1954.

[19] P. W. Higgs, "Broken symmetries and the masses of gauge bosons," *Phys. Rev. Lett.*, vol. 13, pp. 508–509, Oct 1964.

[20] L. Faddeev and V. Popov, "Feynman diagrams for the yang-mills field," *Physics Letters B*, vol. 25, no. 1, pp. 29 – 30, 1967.

[21] D. J. Gross and F. Wilczek, "Ultraviolet behavior of non-abelian gauge theories," *Phys. Rev. Lett.*, vol. 30, pp. 1343–1346, Jun 1973.

[22] M. Dordevic, "Standard Model physics results from ATLAS and CMS," Tech. Rep. CMS-CR-2014-251, CERN, Geneva, Oct 2014.

[23] "The history of qcd — cern courier." `http://cerncourier.com/cws/article/cern/50796`, 2015.

[24] R. Gupta, "Introduction to lattice QCD: Course," pp. 83–219, 1997.

[25] A. Ukawa, "Kenneth Wilson and lattice QCD," 2015.

[26] L. Evans and P. Bryant, "Lhc machine," *Journal of Instrumentation*, vol. 3, no. 08, p. S08001, 2008.

[27] G. Landsberg, "LHC: Past, Present, and Future," 2013.

[28] "Atlas experiment@2015 cern." `http://www.atlas.ch/photos/index.html`, 2015.

[29] G. Aad *et al.*, "Observation of a new particle in the search for the Standard Model Higgs boson with the ATLAS detector at the LHC," *Phys.Lett.*, vol. B716, pp. 1–29, 2012.

[30] R. Bruce, G. Arduini, S. Fartoukh, M. Giovannozzi, M. Lamont, *et al.*, "Baseline LHC machine parameters and configuration of the 2015 proton run," 2014.

[31] "Future prospects for higgs measurements at lhc run 2+3." `http://www.nikhef.nl/pub/BND2014/projects/ILC-vs-LHC-HL/LHC_Aspen_2014_Kroha.pdf`, 2014.

[32] T. A. Collaboration, “The atlas experiment at the cern large hadron collider,” *Journal of Instrumentation*, vol. 3, no. 08, p. S08003, 2008.

[33] *Expected performance of the ATLAS experiment: detector, trigger and physics.* Geneva: CERN, 2009.

[34] E. Halkiadakis, “Proceedings for TASI 2009 Summer School on ’Physics of the Large and the Small’: Introduction to the LHC experiments,” 2010.

[35] T. D. Lee and M. Nauenberg, “Degenerate systems and mass singularities,” *Phys. Rev.*, vol. 133, pp. B1549–B1562, Mar 1964.

[36] T. Kinoshita, “Mass singularities of feynman amplitudes,” *Journal of Mathematical Physics*, vol. 3, no. 4, 1962.

[37] G. Aad *et al.*, “Expected Performance of the ATLAS Experiment - Detector, Trigger and Physics,” 2009.

[38] B. Isildak, “Measurement of the differential dijet production cross section in proton-proton collisions at $\sqrt{s} = 7$ tev,” 2013.

[39] M. Cacciari, G. P. Salam, and G. Soyez, “The Anti-k(t) jet clustering algorithm,” *JHEP*, vol. 0804, p. 063, 2008.

[40] “Dzero final runiia jet energy scale.” `http://www-d0.fnal.gov/phys_id/jes/public_RunIIa/`, 2015.